

Supplemental Information for Revealing the Potential of Luminescent Solar Concentrators in Real-World Environments

Tomi Baikie, Benjamin Daiber, Emil Kensington, James Xiao, Neil Greenham, Bruno Ehrler, Akshay Rao

Contents

1 LAD	2
1.1 Neural Net	3
1.2 LAD Undersampling	3
2 Ray Tracing	6
2.1 Reflection, Refraction and Transmission	6
2.2 LSC Chromophore Concentration	11
2.3 Directional Emission	11
2.4 Back Reflectors	12
2.5 Experimental Verification	13
2.6 Tandem LSC	15
2.7 Dispersion	15
3 Silicon solar cell model	16
3.1 J_G - Generation Current Density	17
3.2 J_{Rad} - Radiative Recombination Current Density	17
3.3 J_{nRad} - Non-Radiative Recombination Current Density	18
3.4 J_{Auger} - Auger Recombination Current Density	18
3.5 Cell Fitting	18
3.5.1 Amsterdam Model Output	19
3.5.2 Colorado Model Output	20
3.6 Window LSC	21
3.7 Model Limitations	21
3.7.1 High Irradiance	21
3.7.2 Temperature	21
3.8 Analytical Model of Angular Reflection Losses	22
4 Photomultiplier LSCs	23
4.1 Quantum Cutting	23
4.2 Singlet Fission	23
5 LSC Size Considerations	24
5.1 Losses as a function of photon pathlength	24
5.2 Solar cell recombination limitations	26
5.3 Recombination limits in the Real World	27
6 Results	29
6.1 Streamgraphs	29
6.1.1 Ray-tracing Streamgraph	30
6.1.2 Complete Simulation Streamgraph	31
6.2 Expanded Geographical Locations	32
6.3 Diffuse and Direct Comparison	34
6.3.1 Comparison to Optical Concentration	34

6.3.2 Comparison to Silicon	35
6.4 Bifacial LSCs	37
6.5 LSC Thicknesses	38
6.6 Other LSC Use Cases	38
6.7 LSC Aesthetics	40
6.8 Further Simulation Results	40
7 Derivations for Cost Metric	46
1 LAD	



Fig. 1 The 12-sided LAD situated at AMOLF. It is encased in a clear spherical protective plastic shell that is heated to prevent a build-up of condensation.

The Light ambient detector (LAD) is a dodecahedron (cube with 12 sides) that has a light sensor on each side (see **SI Figure 1**). The light sensor can record the intensity of red, green, blue and IR light and the temperature and is calibrated using a AM1.5 solar simulator which in turn is calibrated with a traceable silicon solar cell. Notably, it does however not record the spectrum of the sunlight. To acquire the solar spectrum, spectral data from a spectroradiometer (EKO-Wiser MS-711) attached to one side of the dodecahedron is used. Concurrent data from both the LAD sensor network and spectroradiometer are used to train a neural net. The LAD is placed in an urban location depicted in **SI Figure 2**. This is a distinction from meteorological sites, where instruments are generally placed in clear open areas.

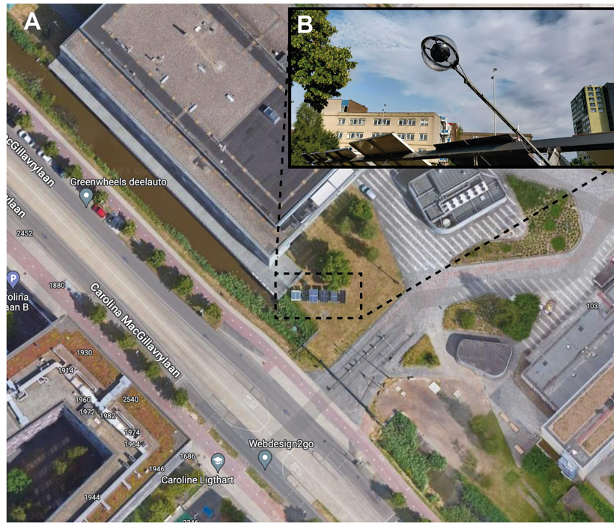


Fig. 2 A - Satellite imagery from Google Maps highlighting the location of the LAD in an urban environment outside the AMOLF institute. Inset B - Photograph of the LAD location.

1.1 Neural Net

The neural net consists of an input layer, of length five, and four hidden layers, including an absolute value layer, and an output layer of length 2048, which represents the predicted spectra for 2048 equally spaced wavelengths. **SI Figure 3** outlines some of the models which were tested and **SI Figure 4** outlines their associated validation losses.

The four hidden layers consist of a linear Layer of length five, a constant layer of length five, a linear layer of length 2048 and an absolute layer. We found that the linear layer of length 2048 dominates the accuracy of the LAD, with only slightly improved performance if the other layers are also included. The training data is the recorded spectrum from the entire year of 2019, in 10 second increments. After 400 rounds of training a plateau has been reached, as can be seen in a plot of the validation loss in **SI Figure 4**.

SI Figure 5 plots four random dates throughout the month of August and the associated measured spectrum recorded from the spectroradiometer attached to one side LAD. We use the same neural net and apply it to the other eleven sides of the LAD, which makes the implicit assumption that the relationship between the LAD sensor array to spectrum is consistent for each sides. The twelve different spectra are then mixed for each angle we wish to predict the spectrum for. Cutting the received irradiance into 10 different angles in altitude and 20 different angles in azimuth results in a solid angle of 8.1° for each spectrum.

1.2 LAD Undersampling

SI Figure 6 highlights that the LAD is unable to record the power in the IR, therefore undersampling the recorded input power in PCE calculations. To account for this in **Figure 4A**, we assume that the recorded power always represents 82.26% of the total input power in the AMOLF case. This value is calculated by dividing the LAD range (200-1200 nm) power (740.485 W/m^2) by the full range (200-4000 nm) input power (900 W/m^2) for AM1.5. No correction is needed for data from Boulder, nor is any correction required for output energy measurements.

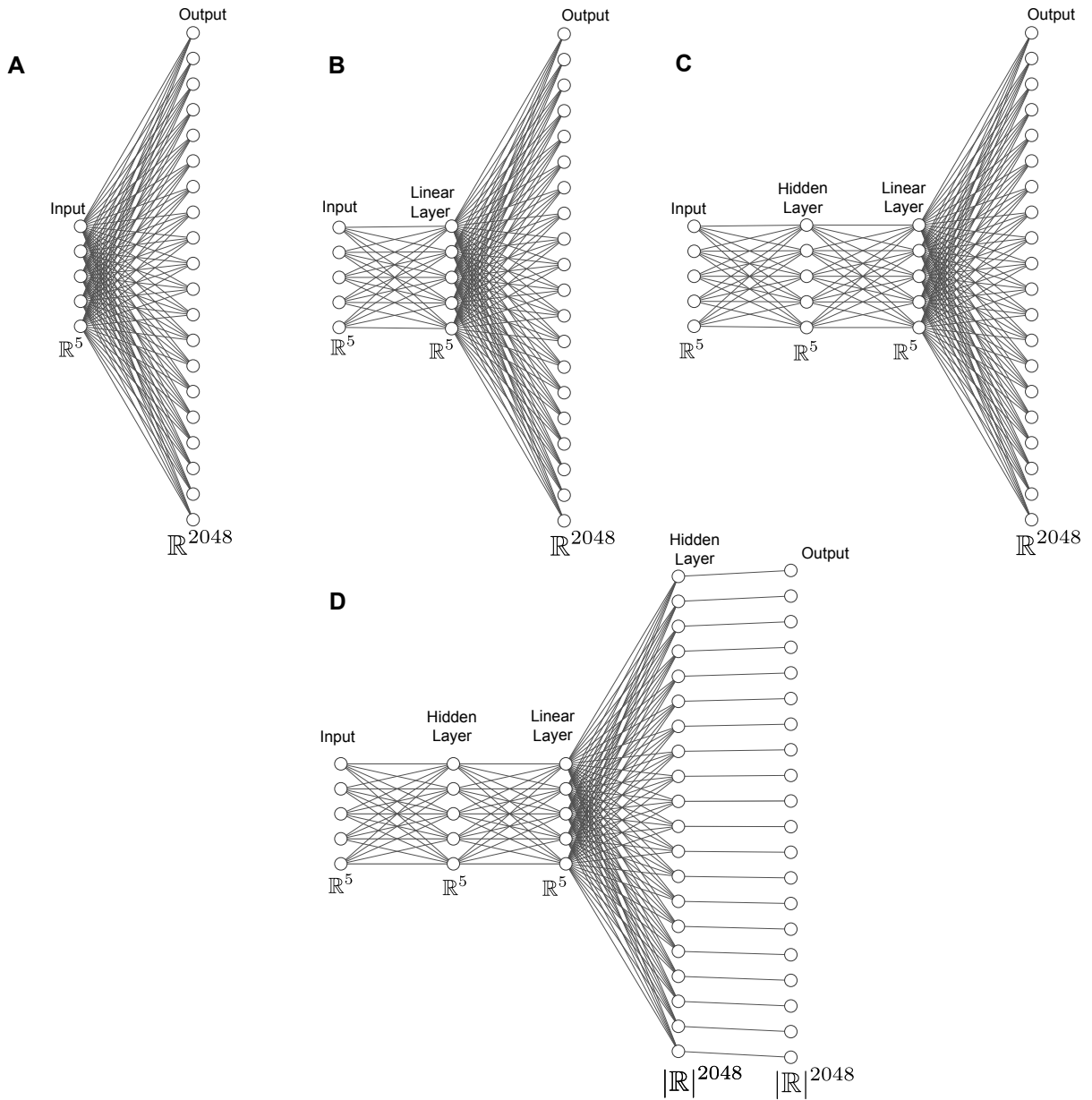


Fig. 3 A selection of neural network chains tested in this project. The 5 inputs correspond to the red, green, blue, IR and temperature photodiodes. Model A is the simplest neural network, attempting to link the inputs directly to the output, which is 2048 nodes, which are linked directly to each wavelength in the calibrated spectrum. Model B adds a linear layer, Model C adds another hidden layer and Model D, the most successful adds on an additional absolute layer, meaning none of the wavelengths are allowed to be negative.

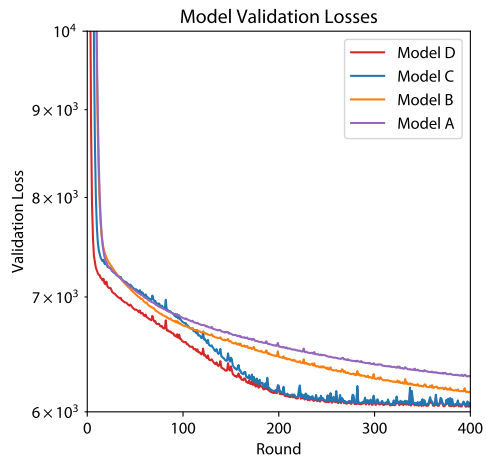


Fig. 4 The validation losses, meaning the difference between the measured spectrum and the neural networks described in SI Figure 3. Model D is the most successful. Training for the primary model continued for longer than 400 rounds, this is simply a subset trained for the month of August.

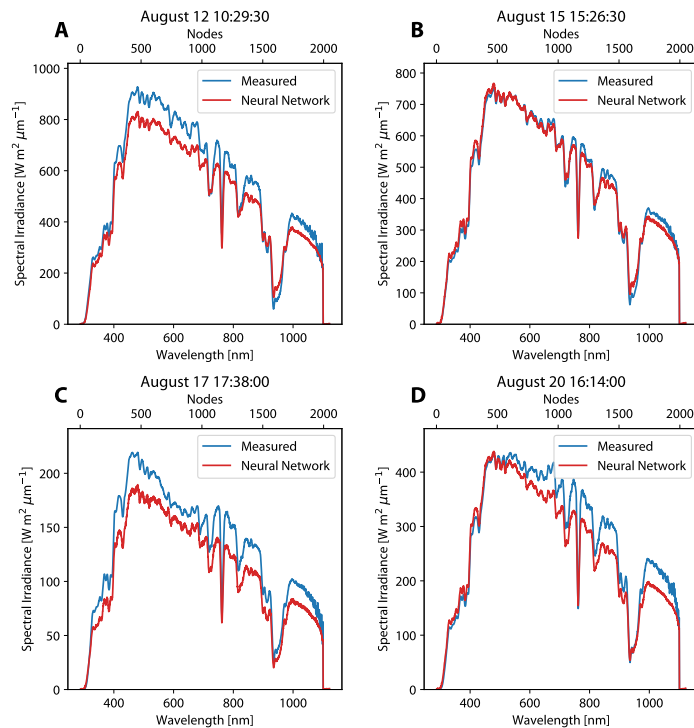


Fig. 5 Plots of the neural network spectral irradiance (in red) and the measured spectra (in blue) for 4 random times, where the times have been chosen to exclude times between sunset and sunrise in August.

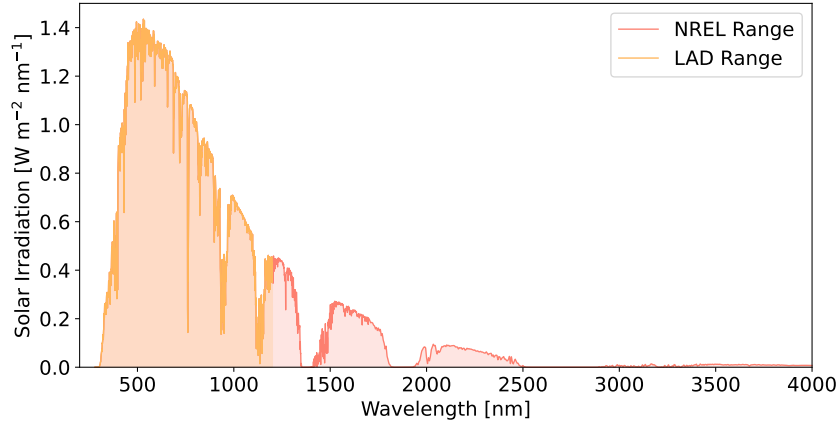


Fig. 6 AM1.5 irradiance plotted as a function of wavelength. Orange region represents the spectral range of the LAD based in Amsterdam, whereas the red range represents the spectral range of the NREL data.

2 Ray Tracing

A raytracing algorithm is outlined below, which allows for the study of any arbitrary LSC. Full code is available at: *insert github link in proof*. The wavelengths of photons impinging on the surface of the LSC are described by a cumulative probability distribution function (CDF), $E_{solar}(P)$, where P is a value between 0 and 1, queried randomly. The chromophores are described by an absorption spectra, given in **Figure 3** in the main text with units of [$M^{-1}cm^{-1}$], and a PL spectrum CDF, $E_{PL}(P)$. The LSC itself is described by a refractive index, n_2 and an absorption spectra, given in units of [cm^{-1}]. The physical dimensions were held constant at 10 cm by 10 cm by 1/3 cm during the simulation unless otherwise noted.

This ray tracing algorithm is unique compared to other reported ray-tracing algorithms as ray-tracing is achieved by generating a logical expression which constrains the geometrical boundary of any arbitrary shape and using a numeric solver to find the intersection of the infinite line given by the position and direction of a photon. As analytical description of the entire LSC surface along with the surface normal is used, any arbitrary shape of LSC may be modelled. The solver computes which computes the intersection between a photon and the LSC uses a numerical Gröbner basis using an efficient monomial ordering, then uses eigensystem methods to extract numerical roots which are returned as intersections. Where multiple roots are found, the intersection closest to the initial point in the direction of motion is chosen.

2.1 Reflection, Refraction and Transmission

To determine the normal to the arbitrary surface, the component normal vectors are determined for all surfaces by component wise numerical differentiation. These normals are referenced when an intersection is a member of the surface within some error of arbitrary machine precision. Thus, for any point on the LSC, a surface a normal can be returned corresponding to that surface without repeating the numerical differentiation for every photon run, lowering computation overheads. If the photon's point is within the LSC region, then the surface normal is reflected about the surface. As in **SI Figure 7**, the refracted ray is determined by

$$\hat{r} = \hat{i} - (\hat{i} \cdot \hat{n})\hat{n} \quad (1)$$

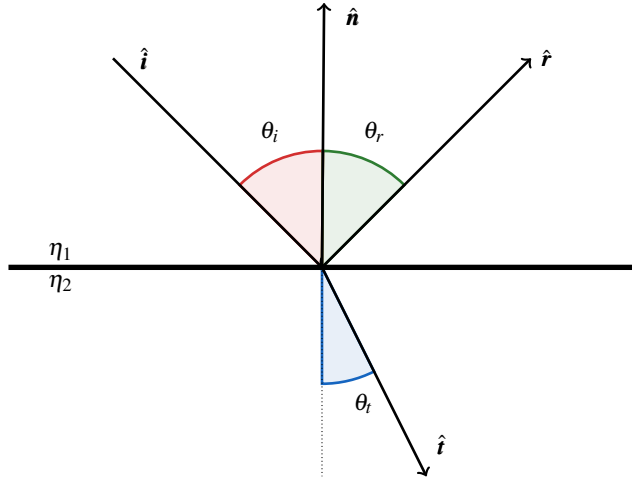


Fig. 7 A ray moving between two materials with refractive indices of n_1 and n_2 . The normalised direction vector of the incident ray is given by \hat{i} . The normalised reflected and transmitted rays are labelled as \hat{r} and \hat{t} respectively. The diagram depicts a scenario where $n_1 < n_2$.

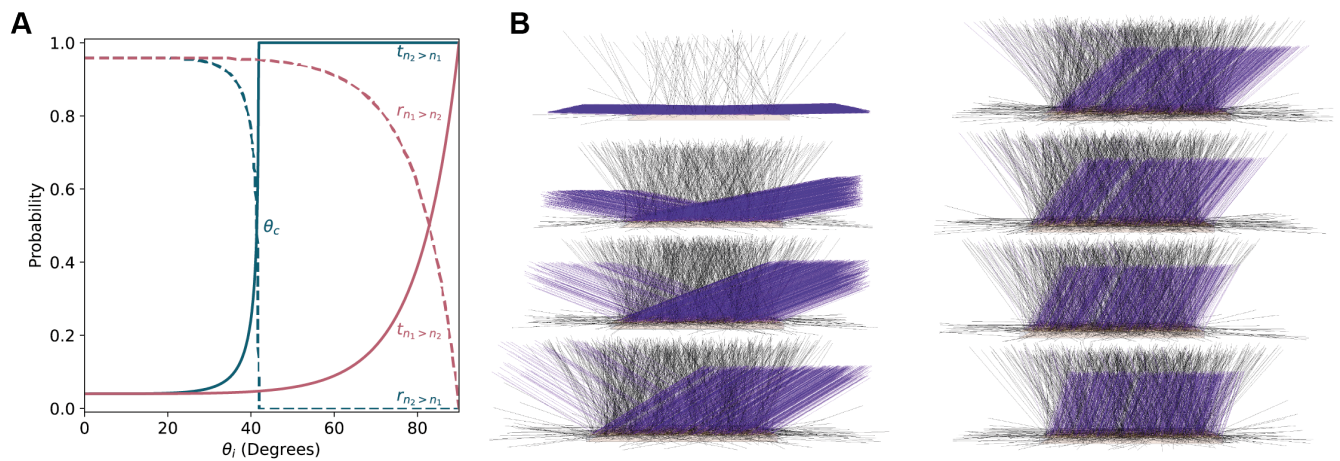


Fig. 8 A - Depicts the probability of reflection (dashed) and refraction (solid) as a function of incident angle θ_i . The red line depicts the situation where $n_1 < n_2$ where $n_1 = 1$ and $n_2 = 1.5$. The blue line depicts the regime when $n_1 = 1.5 > n_2 = 1$. At a certain critical angle $\theta_i = \theta_c$, the reflected vector \hat{r} no longer exists. B - Results from the dot LSC described in the main text with 420 nm illumination and IR emission (in black) as a series of different input angles.

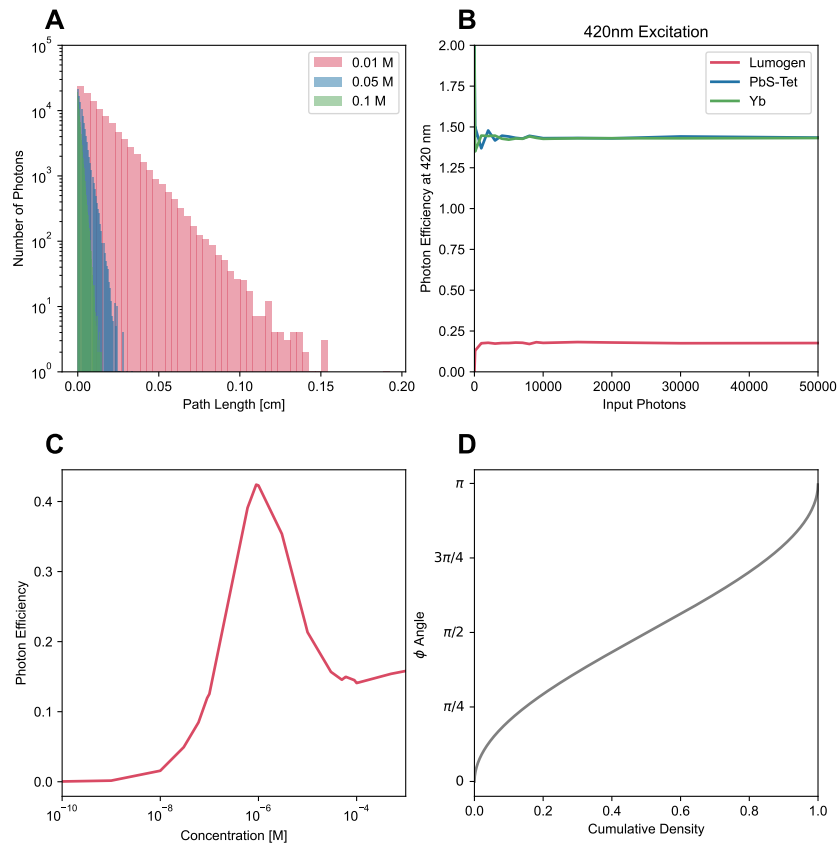


Fig. 9 A - Depicts photon pathlengths for the tetracene PbS systems at different concentrations, where 100000 photons have been modelled. B - Photon efficiency at 420 nm Excitation as a function of number of photons. At low number of photons the result fluctuates, whereas at high number of photons the result of the model is stable. C - Determining the optimal concentration for the lumogen LSC. D - Cumulative probability of azimuthal angle (ϕ) for an isotropic emitter.

where \mathbf{n} is the surface normal unit vector and $\hat{\mathbf{i}}$ is the unit vector in direction of the photon. Similarly, the reflected ray is given by

$$\hat{\mathbf{i}} = \frac{n_1}{n_2} \hat{\mathbf{i}} + \left(\frac{n_1}{n_2} \cos(\theta_i) - \sqrt{1 - \sin^2(\theta_t)} \right) \hat{\mathbf{n}}. \quad (2)$$

Where,

$$\cos(\theta_i) = -\hat{\mathbf{i}} \cdot \hat{\mathbf{n}}, \quad (3)$$

and

$$\sin^2(\theta_t) = \left(\frac{n_1}{n_2} \right)^2 (1 - \cos^2(\theta_i)). \quad (4)$$

In the case, $n_1 > n_2$, the refracted vector does not exist above the critical angle, where the critical angle is given by

$$\theta_c = \sin^{-1} \left(\frac{n_2}{n_1} \right) \iff \eta_1 > \eta_2. \quad (5)$$

The probability for reflection or refraction is given by Fresnel's laws,

$$r_{\perp}(\theta_i) = \left(\frac{n_1 \cos(\theta_i) - n_2 \cos(\theta_t)}{n_1 \cos(\theta_i) + n_2 \cos(\theta_t)} \right)^2 \quad r_{\parallel}(\theta_i) = \left(\frac{n_2 \cos(\theta_i) - n_1 \cos(\theta_t)}{n_2 \cos(\theta_i) + n_1 \cos(\theta_t)} \right)^2 \quad (6)$$

with

$$t_{\perp} = 1 - r_{\perp}, \quad t_{\parallel} = 1 - r_{\parallel}. \quad (7)$$

For unpolarised light the probability of transmission or reflection is then the average of the two probabilities:

$$P_{\text{refraction}} = \frac{1}{2}(t_{\perp} + t_{\parallel}), \quad P_{\text{reflection}} = \frac{1}{2}(r_{\perp} + r_{\parallel}). \quad (8)$$

Representative probabilities are given in **SI Figure 8** for refractive indices of $n_1 = 1$ and $n_2 = 1.5$. Once a ray is transmitted into the LSC, the path length of the photon is determined by

$$l(\lambda) = -\frac{\log_{10}(\text{Rand}[]) \eta_c(\lambda) c + \eta_{LSC}(\lambda)}{\eta_c(\lambda) c + \eta_{LSC}(\lambda)} \quad (9)$$

where l is the path length l , $\text{Rand}[]$ is a random real generated by 0 and 1, $\eta_c(\lambda)$ is the extinction coefficient multiplied by the molar concentration c , η_{LSC} is the wavelength dependent absorption of the substrate. Contained within the unsophisticated function, `While[1<2]`, the photon is allowed to travel within the LSC, with the possibility of reflectance or refraction calculated at each intersection with the LSC until the euclidean distance traveled is equal to the path length. If the photon intersects one of the sides with the solar cell attached, this the recorded and the simulation moves onto the next photon. If the distance travelled is equal to the path length, the photon may either undergo a nonradiative decay

(NRD), an emission or an emission and a photon multiplicative event (PME), the probabilities of which depend on the chromophore. Photon pathlengths for the Tet-PbS system are given in **SI Figure 9A** for various concentrations.

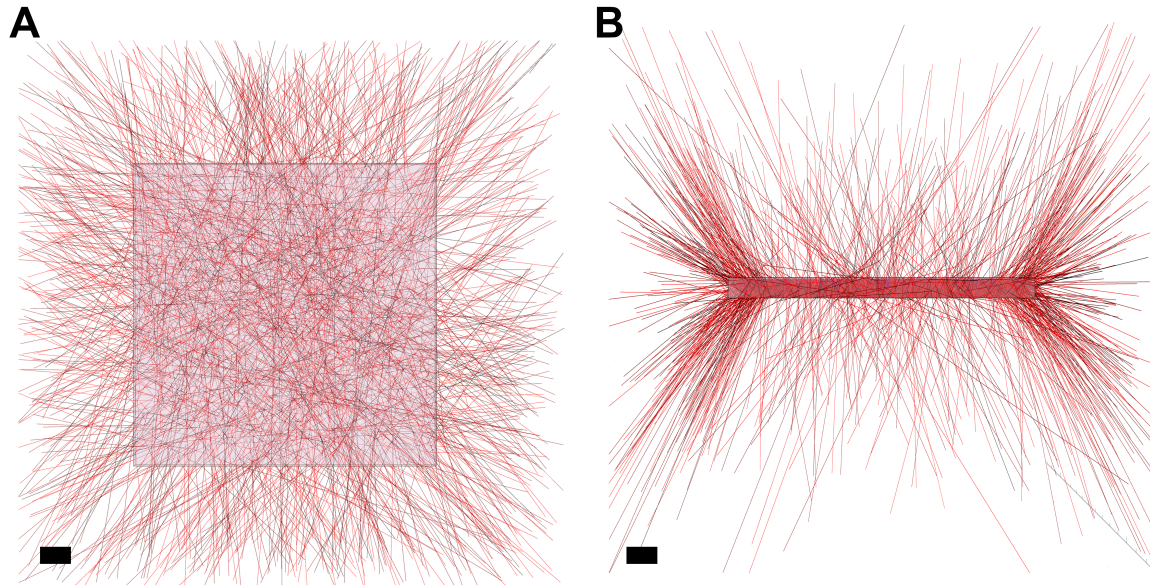


Fig. 10 Graphical representations of 1000 photons which impinged on the solar cell surfaces from modelling a Lumogen system where the edges have been expanded for clarity. Scale bar is 1 cm

If photon undergoes a NRD event, this is recorded and the simulation moves onto the next photon. If an emission event is determined, a new path length and direction is determined and the process repeats until the photon leaves the LSC, is absorbed by a solar cell, or undergoes a NRD event. If PM events are enabled, the simulation will leave a marker that a PM event took place at the emission location, and will return to the point at the end of the original photon list to run these PM photons.

The rest of the functions presented within the code manage running the simulation on multiple cores, as no photon is dependent on another, this parallelisation is relatively trivial. There are also functions to generate graphical representations of the data, such as those in **SI Figure 10**, as well functions which list the photons which exited from the solar cell sides to determine the optical efficiencies and the spectrum of these photons. The final function converts the code into a format suitable for high performance clusters.

As the simulation is a Monte Carlo simulation, meaning it relies on random sampling to arrive at a solution. The simulation particularly relies on randomness upon deciding the photon path at the interface of the LSC, determining the path length and properly sampling the incident spectrum and chromophore emission spectrum. Therefore a number of repeated runs will be required to extract statistically significant results. **SI Figure 9B** outlines how the photon efficiency changes as function of the number of photons sampled. We find that sampling 10000 photons gives a consistent result with less than < 1% variance. For each wavelength, the impingement angle of photons is varied in 1 degree steps, due to the four way symmetry of this particular LSC, we need only study the lateral angle from 0 to $\pi/2$ to be able to study all angles from the weighted spectra impinging on each solar cell side of the LSC.

2.2 LSC Chromophore Concentration

SI Figure 9C plots the concentration dependence as a function of internal efficiency for the lumogen LSC. Therefore, we use an optimised chromophore concentration of $1 \mu\text{M}$. For diffuse light, the average pathlength is

$$\bar{l} = \frac{d}{\sin(\frac{\pi}{2} - 0.3)} = 0.35, \quad (10)$$

where d is the thickness of the LSC, in our case $1/3 \text{ cm}$, hence $\bar{l} = 0.35$. To allow for 99.9% absorbance in the systems with no absorption and emission overlap, the concentration of the LSC must satisfy

$$0.35 \varepsilon c > \log_{10}[1/0.001], \quad (11)$$

In the case of the Yb system the average absorbance is $42000 \text{ M}^{-1} \text{ cm}^{-1}$, hence a concentration of $300 \mu\text{M}$. Similarly, for the tetracene system, the average absorbance is $3600 \text{ M}^{-1} \text{ cm}^{-1}$, which is equivalent to 3 mM . For the imagined PM-LSC, this is $170 \mu\text{M}$ ($50\text{k M}^{-1} \text{ cm}^{-1}$), and for the imagined quantum dot LSC, this is $400 \mu\text{M}$ ($20\text{k M}^{-1} \text{ cm}^{-1}$).

2.3 Directional Emission

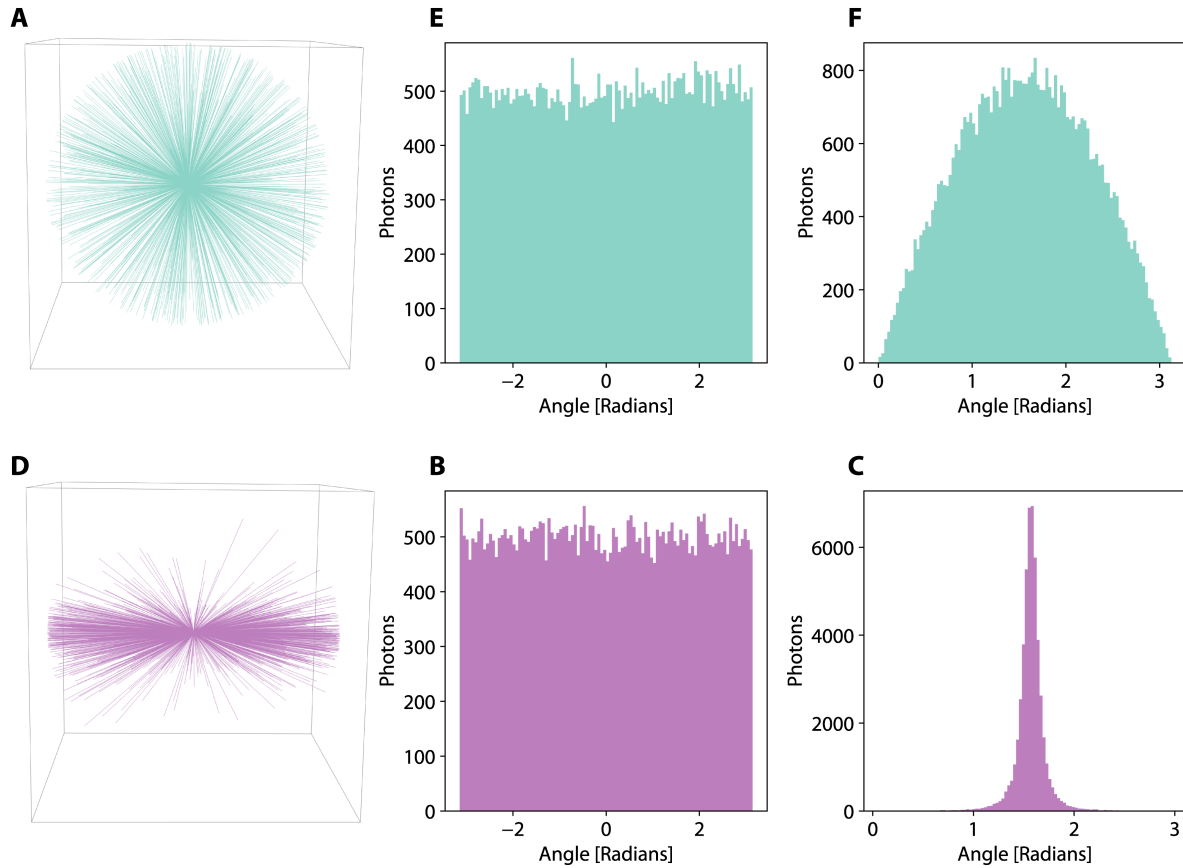


Fig. 11 A & D - Plots the direction vector of 1000 photons for an isotropic emitter in green and the anisotropic emission used in the simulations in red, B & E- is a histogram of 50000 photons the azimuthal angle for both cases, and C & F is the equivalent histogram for the polar angle.

Generally, experimental demonstrations LSC, such as the dye, quantum dots and randomly orientated perovskite

nanocrystals described in the main text, exhibit isotropic emission. The azimuthal angle ($\theta \in [-\pi, \pi]$), and the azimuthal angle ($\phi \in [0, \pi]$) are related to the direction vector of the photon by

$$\begin{aligned} x &= \cos(\theta) \sin(\phi) \\ y &= \sin(\theta) \sin(\phi) \\ z &= \cos(\phi) \end{aligned} \tag{12}$$

where the direction of the photon is given by $\vec{d} = \frac{(x,y,z)}{\|(x,y,z)\|}$. For isotropic emission ϕ is sampled from the CDF in **SI Figure ??D** and θ given by

$$\theta = 2\pi(\text{RandomReal}[]) \tag{13}$$

where `RandomReal[]` is a random value between 0 and 1.

To account for mirrors, DBRs and anisotropic emitters, we alter the emission direction by scaling the z axis by 0.1 and then normalising, i.e. if the direction is given by (x,y,z) , then the anisotropic emission is given by $|(x,y,0.1z)|$. **SI Figure 11** plots the angular distribution of emission for the isotropic and anisotropic chromophores. The azimuthal angle, θ , and the polar angle, ϕ in **SI Figure 11** are determined by

$$\begin{aligned} r &= \sqrt{x^2 + y^2 + z^2} \\ \theta &= \tan^{-1}\left(\frac{y}{x}\right) \\ \phi &= \cos^{-1}\left(\frac{z}{r}\right) \end{aligned}$$

where the inverse tangent accounts for which quadrant (x,y,z) is in.

2.4 Back Reflectors

SI Figure 12 models a Lumogen LSC without any reflective back edge, a scattering back reflector, reflective back reflector and with directional emission chromophore. **SI Figure 12** also shows the pathlength of a random portion of the photon which successfully travel to the edges of the LSC and are absorbed by the PV. It is clear that the directionally emitting LSC reduces the pathlength of the photons, reducing losses without the need for a back reflector. Therefore, the directional emitter represents an upper bound in efficiency as this minimises photon pathlength, as reflections act to increase the photon pathlength and many LSC losses in the Lumogen LSC are a function of photon pathlength. Therefore, we conclude that all back reflectors or Bragg reflectors are likely only increase losses relative to directional emitters if losses are a function of pathlength and as such directional emission will represent the efficiency limit.

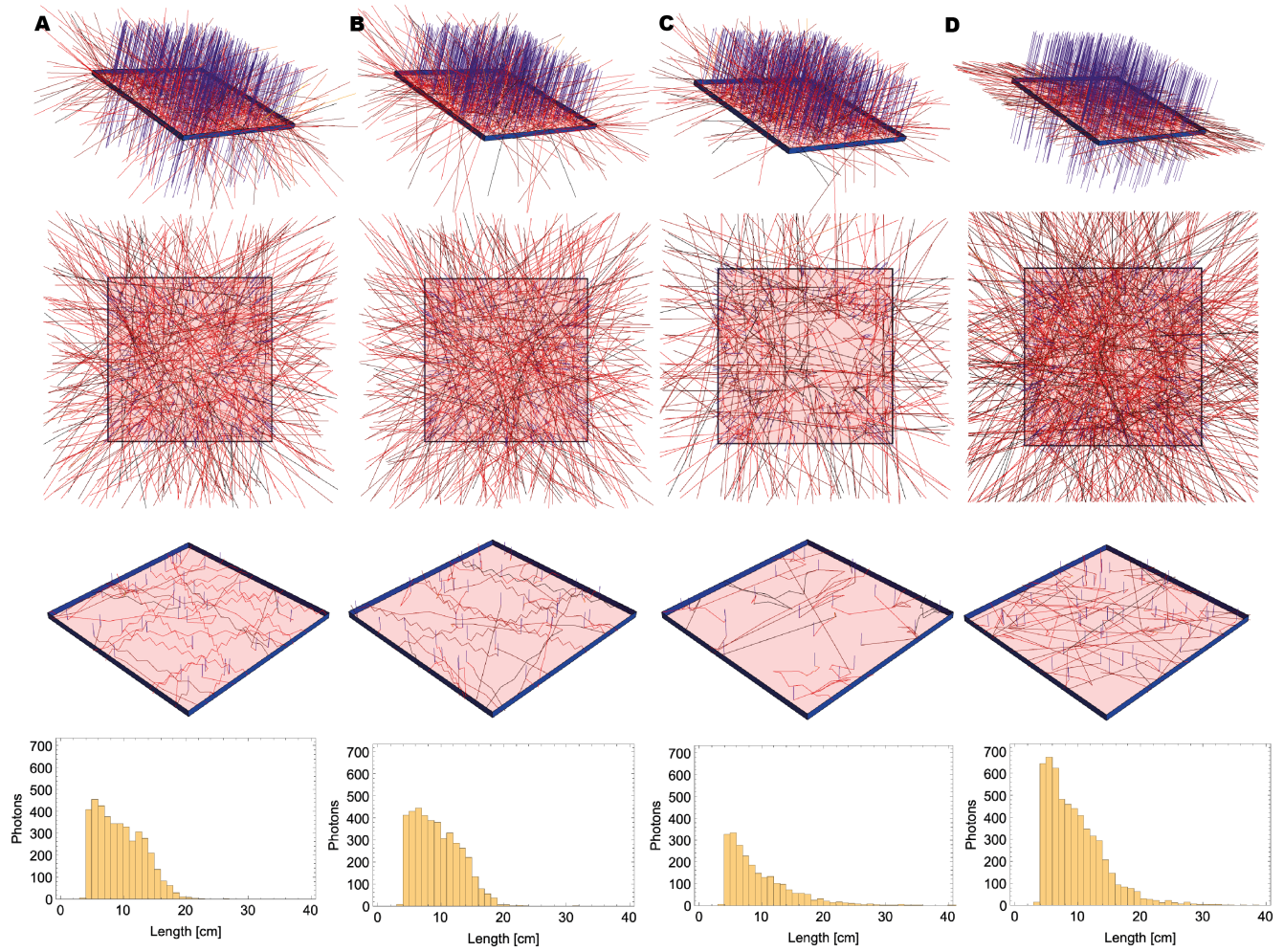


Fig. 12 Effect of back reflectors A – Normal Lumogen LSC with concentration (0.4 mM) such that it does that does not absorb all photons over the depth of the LSC. B – Lumogen LSC with reflective back surface. C – LSC with perfectly scattering back surface. D – LSC with directional emitter as described in the main text (also see SI Section 2.3). Top graphic plots 500 photons, where transmission is only observed in the A and D cases. Second graphics represents a 10th of the photons that impinge on the edges of the LSC. The third from top graphic represents the 1/100th of the photons that make it to the edges, in A, B and C traditional total internal reflection (the “zig-zags”) may be observed, transmitting photons to the edge. The bottom graphic plots the photon pathlength of the photons that impinge on solar cell edges, which shows that the directional emitting LSC representing a limiting case with the highest photon efficiency, but also the lowest pathlength.

2.5 Experimental Verification

The Lumogen LSC in the main text was manufactured and then measured as a function of average photon pathlength using spatially resolved measurements¹. As in **SI Figure 13** we recover with pleasing accuracy the photon losses as a function of pathlength from the simulation, as well as a close match to the optical efficiency¹. We suggest that the slight variation in spectral shape may be due to increased scattering, rather than photon recycling, in the LSC which acts to increase the reabsorption probability, which we do not consider within the simulation combined with the fact that upon reabsorption the PL need not be red-shifted within the simulation, but is randomly picked from the emission spectra of the chromophore (other than in the PM-LSC). We also note our simulation matches other experimentally recovered optical efficiencies. This result may not be surprising as only the implementation, rather than any changes of the physical underpinning of the method of the monte-carlo based raytracing algorithms has been made in this work and these algorithms which have long

used to model and recover experimental results^{2–7}.

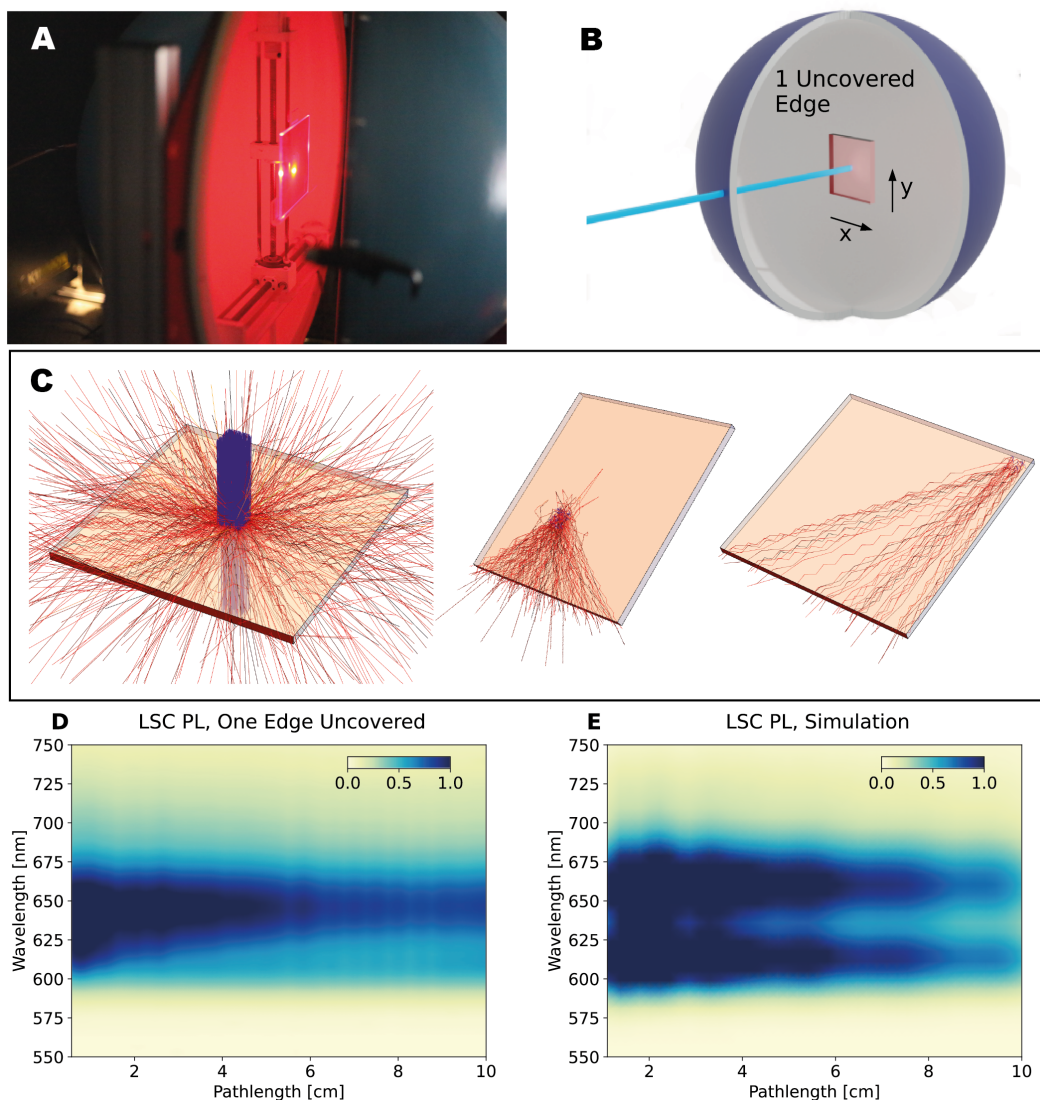


Fig. 13 A - Photograph of spatially resolved LSC measurement B - Adapted from Baikie *et al.*¹, highlighting how the measurement is spatially resolved. C - Replicating the experimental arrangement within the simulation, where the laser (in blue) is rastered across the LSC and the photon output measured. D - Experimental results contrasted with E - simulation results. Photon losses as a function of illumination position are approximately the same.

2.6 Tandem LSC

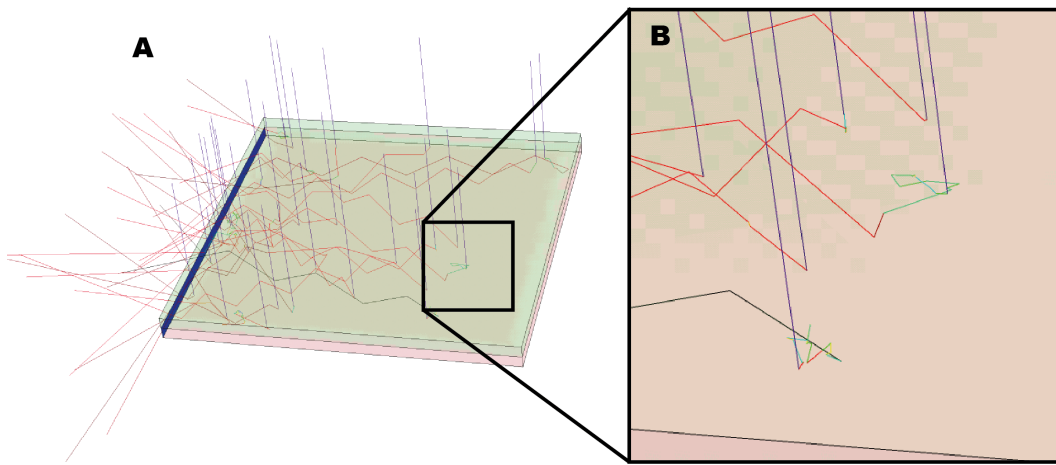


Fig. 14 A – Tandem LSC, with a lumogen 305 LSC in tandem (with no optical barrier) with a similar LSC, but emission is shifted by 100 nm to the green. Only the first 50 photons that have been transmitted to the blue edge (seen on the left of the red LSC) have been plotted. B – Depicts a photon which is absorbed on the top surface and reabsorbed on red tandem side.

LSCs may be deposited layers, composite, single layer tandems, sandwich (effectively two LSCs). With the maintext we describe composite LSC, where the chromophores are incorporated within the matrix. It is readily possible to model a tandem from the ray-tracing perspective (see **SI Figure 14**), which may prove useful in optimising the concentration of chromophores for tandem LSCs. However, there remains an open and unresolved question from the circuit modelling front on tandems themselves, which is beyond the scope of this work.

The optimum bandgap for a tandem applied to silicon is likely to be around 1.75 eV⁸, which has been demonstrated to improve the silicon PV energy capture efficiencies. These studies offer some insights into LSC tandem design, however, these tandem solar cells do not have well established Auger recombination rates, a fundamental limitation of a PV applied to LSCs. This leaves an important unknown in our circuit model. Notwithstanding the Auger recombination rate question there remain arguments for two-terminal monolithically integrated, three-terminal, four-terminal mechanically stacked and four-terminal optical spectral splitting tandems, which remains beyond the scope of this work, and may be rather complicated in the LSC context⁹.

2.7 Dispersion

SI Figure 15 highlights the lack of dispersion in some materials and operating region we discuss in the main text, indeed, the largest fractional difference between different wavelengths (blue and IR flight) is less than 0.1% in BK-7 glass. Within the simulation it is trivial to alter the simulation to consider these effects. This is likely to be important for non-rectangular LSCs or otherwise non-symmetric LSCs (which we do not consider in detail here) as if the the second face will be at some angle to the first, this will act to accentuate the dispersion effect (as in triangular prisms).

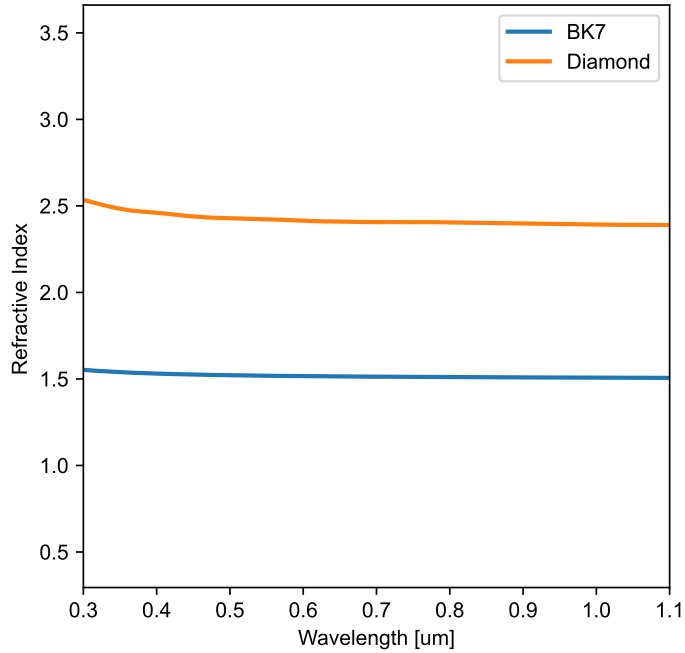


Fig. 15 Wavelength dependent refractive index of select materials, highlighting little changes in the regions important in this work.¹⁰

3 Silicon solar cell model

The model utilised is an extension of a silicon cell model reported by Futscher et al.^{11–13}. This model requires an input of the LSC edge emission spectra and irradiance and outputs the IV curve for the system, power conversion efficiencies (PCE) and kilo-Watt hour (kWh).

We model a record silicon solar cell, in this case a heterojunction interdigitated back contact (HJ-IBC) Si cell, with an efficiency of 26.7% in standard test conditions¹⁴. To model this specific cell, we use the reported external quantum efficiency (*EQE*) and thickness (*L*) of the cell (200 micron). The cell used was 180cm² in area, and we make the explicit assumption that there is no notional loss in efficiency upon application to the thin ($\approx 3\text{cm}^2$) edges of the modelled LSC.

We make the depletion and superposition approximations as detailed by Nelson¹⁵. The depletion approximation assumes that quasi-Fermi levels are constant across the depletion region, the electric field varies linearly across the depletion region and the junction contains no free carriers. The superposition approximation assumes that recombination rates are linear in the neutral regions for minority carrier densities. This model builds upon the well known Shockley-Queisser limit¹⁶ by introducing additional losses due to non-radiative recombination arising from Shockley-Read-Hall (SRH) recombination, Auger recombination, and parasitic resistances.

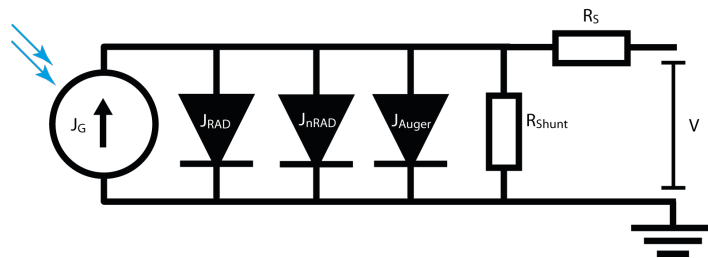


Fig. 16 Equivalent circuit of the Si solar cell model, with black arrows indicating the flow of current. Photons (shown in blue) give rise to a generation current (J_G) which is countered by losses through radiative, non-radiative, and Auger recombination, along with loss from shunt resistance.

We characterise the cell as a set of diodes, as shown in the equivalent circuit diagram in SI Figure 16, where each form of carrier recombination contributes to a loss in current density, $J(V)$, with units of amps per metre squared, at a given voltage, V . The equation,

$$J(V) = J_G(EQE, \Gamma) - J_{Rad}(V, R_S, T) - J_{nRad}(V, R_S, T) - J_{Auger}(V, R_S, L, T) - \frac{V + J R_S}{R_{Shunt}} \quad (14)$$

describes this relationship, where $J(V)$ measured current density, J_{Auger} is the auger recombination current density, J_{Rad} is the radiative recombination current density, J_{nRad} is non-radiative recombination, and $\frac{V + J R_S}{R_{Shunt}}$ is the current lost due to parasitic shunt resistance (R_{Shunt}).

SI Equation 14 produces an J-V curve, from which we can determine the maximum power point (MPP). The power conversion efficiency of the cell is then

$$\eta_{PCE} = \frac{P_{Out}}{P_{In}}, \quad (15)$$

where P_{Out} is the power out of the cell and P_{In} is the total spectral irradiance incident on the cell.

3.1 J_G - Generation Current Density

The generation current is determined from multiplication of the external quantum efficiency per unit energy of the solar cell by the spectral flux per unit area per unit energy ($\Gamma(E)$),

$$J_G = q \int_{E_{min}}^{E_{max}} EQE(E) \Gamma(E) dE, \quad (16)$$

where q is the elementary charge and EQE is the external quantum efficiency of the solar cell.

3.2 J_{Rad} - Radiative Recombination Current Density

The current loss associated with radiative recombination is given by the diode equation

$$J_{Rad} = J_{Rad,0} \left(\exp \left(\frac{V + I R_{Series}}{k_B T} \right) - 1 \right) \quad (17)$$

where

$$J_{Rad,0} = \frac{2 \pi q}{c^2 h^3} \int_{E_G}^{E_{max}} \frac{E^2}{\exp \left(\frac{E}{k_B T} \right) - 1} dE \quad (18)$$

represents the dark recombination current density. J_{Rad} is dependent only on the temperature and the bandgap of the semiconductor material.

3.3 J_{nRad} - Non-Radiative Recombination Current Density

J_{nRad} is mediated by the likelihood of an excited electron relaxing via a trap state. It increases as the diffusion constant increases and diffusion lengths and dopant densities decrease. In our model J_{nRad} is given by

$$J_{\text{nRad}} = J_{\text{nRad},0} n_i(T)^2 \left(\exp \left(\frac{V + J R_{\text{Series}}}{k_B T} \right) - 1 \right), \quad (19)$$

where $n_i(T)$ in $[\text{m}^{-3}]$ is the temperature-dependant intrinsic charge carrier density. Misiakos and Tsamakis give an empirical equation for the temperature-dependence of the intrinsic charge carrier density in Si, as¹⁷

$$n_i = 5.29 \times 10^{19} \left(\frac{T}{300 \text{ K}} \right)^{2.54} \exp \left(\frac{-6726}{T} \right). \quad (20)$$

$J_{\text{nRad},0}$ is the non-radiative recombination constant given by

$$J_{\text{nRad},0} = q \left(\frac{D_n}{N_a L_n} + \frac{D_p}{N_d L_p} \right), \quad (21)$$

where D_n and D_p are the diffusion constants for electrons and holes, N_a and N_d are the density of acceptor and donor doping densities, and L_n and L_p are the diffusion lengths of electrons and holes respectively. We, however, treat $J_{\text{nRad},0}$ as a constant reflecting the specifics of the solar cell, and treat it as a fitting variable.

3.4 J_{Auger} - Auger Recombination Current Density

J_{Auger} is given by

$$J_{\text{Auger}} = q L C(T) n_i^3 \left(\exp \left(\frac{3(V + I R_{\text{Series}})}{2 k_B T} \right) - 1 \right), \quad (22)$$

where C in $\left[\frac{\text{m}^6}{\text{s}} \right]$ is the Auger coefficient given by¹⁸

$$C = 3.79 \times 10^{-43} \sqrt{\frac{T}{300}}, \quad (23)$$

and the silicon bandgap temperature dependence is given by Varshni¹⁹

$$E_G = E_{G,0} - \frac{\xi T^2}{T + \chi}. \quad (24)$$

where $E_{G,0} = 1.17 \text{ eV}$, $\xi = 4.73 \times 10^{-4}$, and $\chi = 636 \text{ K}$ as given by Sze²⁰.

3.5 Cell Fitting

From **SI Figure 17**, we fit **SI Equation 14** assuming standard test conditions and treat $J_{\text{nRad},0}$, R_{Series} and R_{Shunt} as fitting variables. The fitted values were determined as $R_{\text{Series}} = 0.08 \Omega \text{ cm}^2$, $R_{\text{Shunt}} = 10000 \Omega \text{ cm}^2$, and $I_{\text{nDad0}} = 1.88485 \times 10^{-42} \text{ A m}^4$.

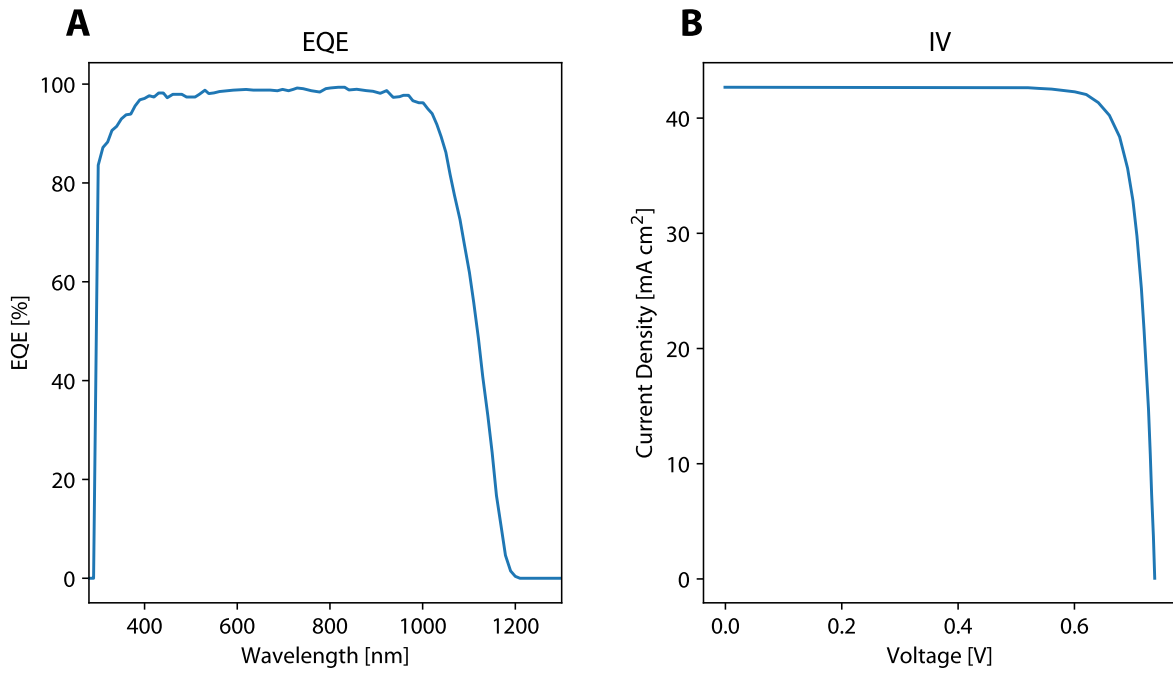


Fig. 17 A- External quantum efficiency (EQE) of the silicon solar cell used in our simulations and - B - J-V characteristic reported by Yoshikawa et al.¹⁴

3.5.1 Amsterdam Model Output

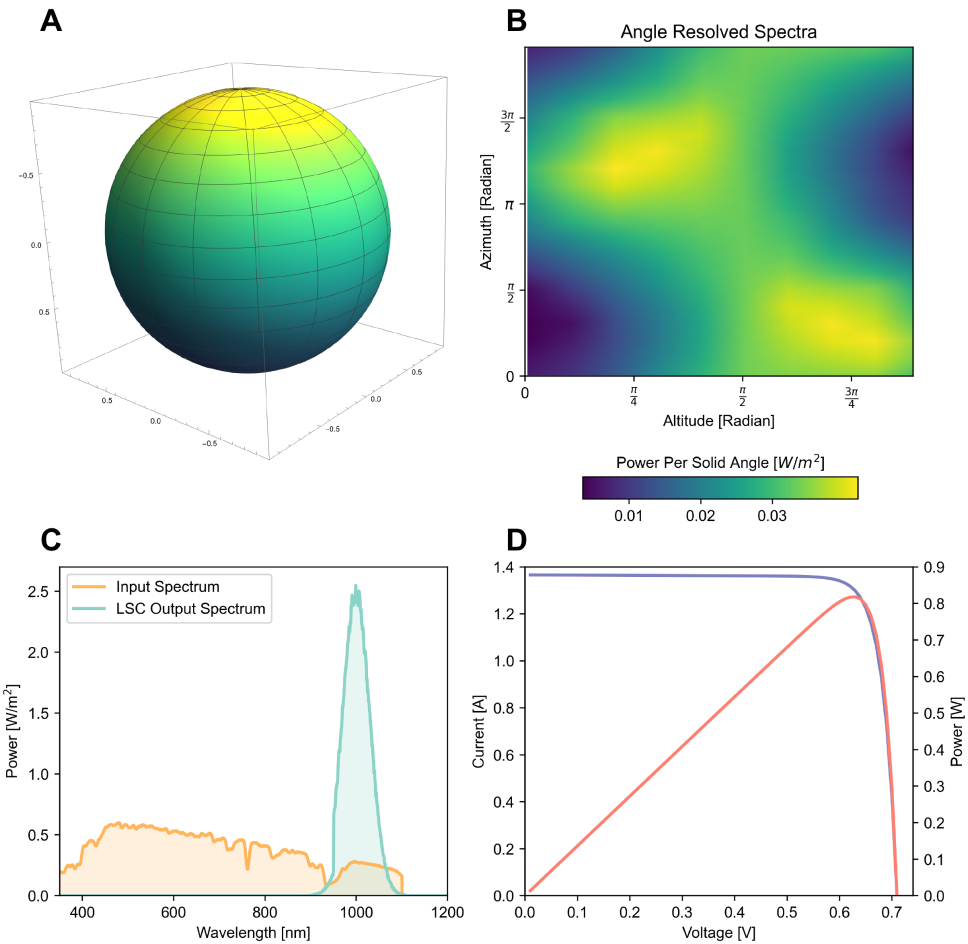


Fig. 18 A & B - Angle resolved spectra recorded with the LAD on Tuesday the 2nd of Jul 2019 at 12:06:32. C - Spectrally resolved input power and LSC output power. D - Silicon solar cell model output, blue curve is the IV characteristic and the red curve plots the power.

The results for a single time point, Tuesday the 2nd of Jul 2019 at 12:06:32, is given in **SI Figure 18**. The input power is 294 W/m^2 , the output power is 179 W/m^2 , giving an LSC PCE of 61%. Note, the jump at 950 nm in the output spectra is due to the absorption of the dot finishing suddenly at 950 nm. The output power spectrum is scaled by the elementary charge and the EQE of the solar cell, to produce a current density, in this case 136.6 A/m^2 . Here the current density has units of per area, which is not the area of the solar cell, but the input surface area of the LSC. Further, the output spectrum is only valid at the dimensions that the raytracing simulation was carried out at. From the current density, the IV characteristic is then produced by application of the model described in **SI Section 3**. For the configuration described in the main text, the output power was determined as 0.81 W. This is therefore a 45.6% PCE when compared to the LSC spectral output, and a total PCE of 27.8% when compared to the input spectrum.

3.5.2 Colorado Model Output

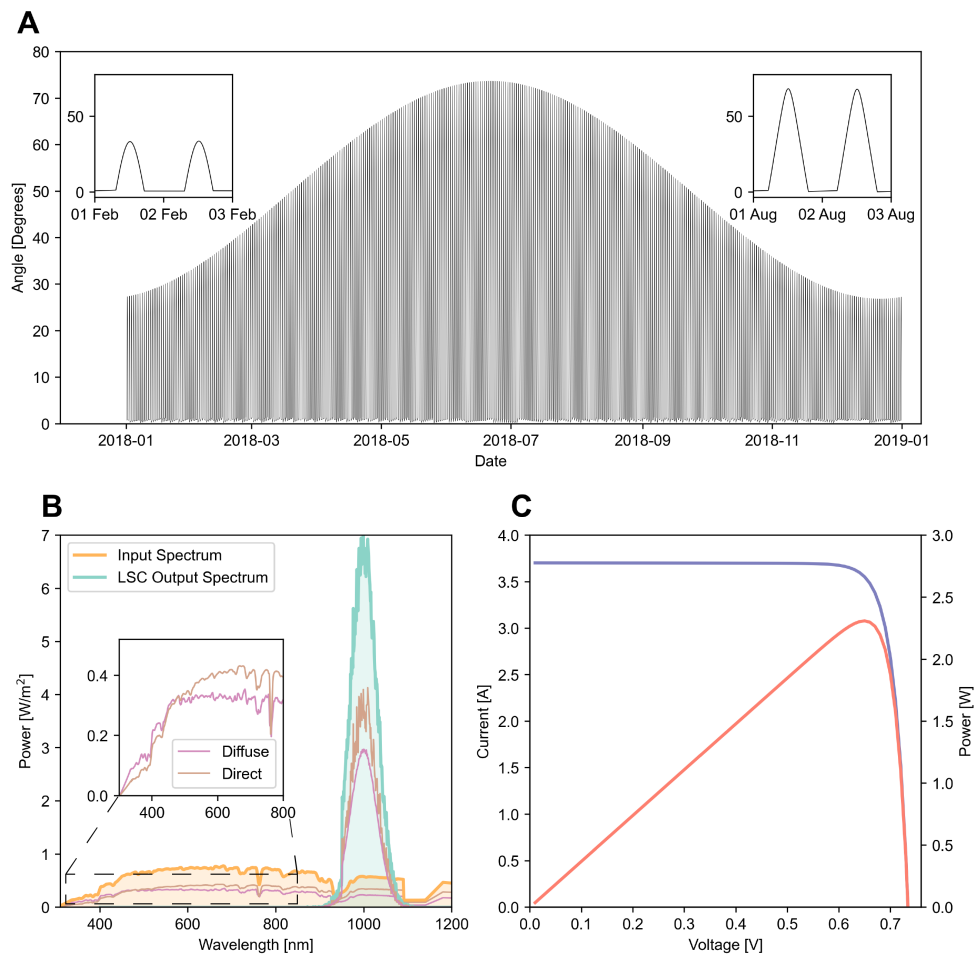


Fig. 19 A - Direct angle over the course of a year mapped onto the ray tracing model for a horizontal LSC. B - Spectrally resolved input power and LSC output power, with diffuse (in purple) and direct (in brown) components overlaid . C - Silicon solar cell model output, blue curve is the IV characteristic and the red curve plots the power.

The results for a single time point, Friday the 20th of Jul 2018 at 14:25:00, is given in **SI Figure 19**. The incident angle of the direct illumination is 55 degrees with respect to the ray tracing algorithm. The input power is 1020 W/m^2 ,

the output power is 486 W/m^2 , giving an LSC PCE of 48%. The input direct and diffuse power is 579 W/m^2 and 441 W/m^2 , respectively. The corresponding LSC output power arising from the direct and diffuse illumination is 271 W/m^2 (79%) and 215 W/m^2 (63%), respectively. The output power spectrum is scaled by the elementary charge and the EQE of the solar cell, to produce a current density, in this case 370.3 A/m^2 . From the current density, the IV characteristic is then produced by application of the model described in **SI Section 3**. For the configuration described in the main text, the output power was determined as 2.3 W. This is therefore a 47.5% PCE when compared to the LSC output, and a total PCE of 22.6% when compared to the input spectrum.

3.6 Window LSC

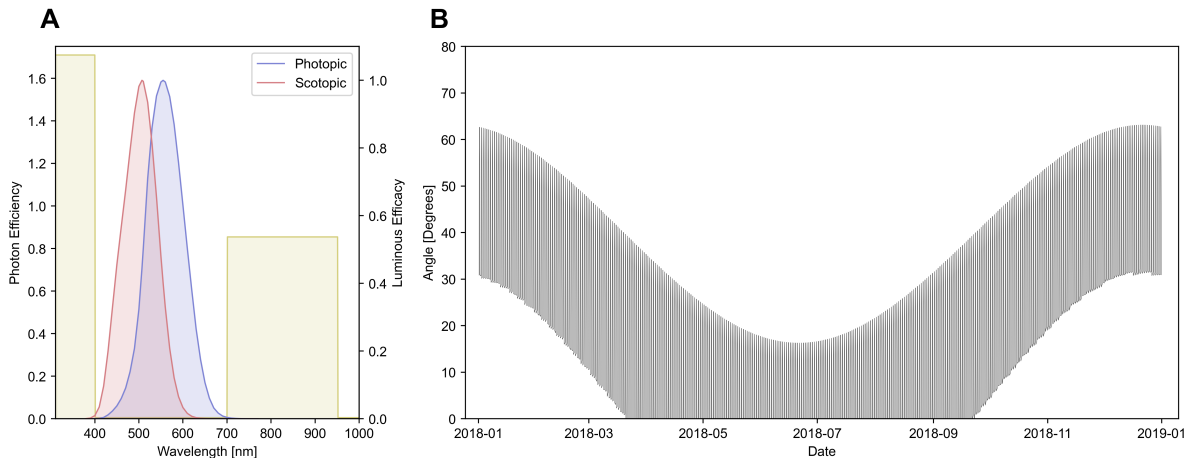


Fig. 20 A - Photon efficiency as a function of wavelength, highlighting the region which passes both the human light-adapted (photopic) case and the dark-adapted (scotopic) luminous efficacy spectra²¹. B - In the Colorado simulation case, as the LSC is now mounted vertically, facing South, at some points of the year, some of the direct spectrum will arrive at angles inaccessible to the LSC.

The window LSC stands vertically and is facing South. It has a absorption spectrum which passes visible light, see **SI Figure 20**). Notably, as the LSC stands vertically as the sun moves higher in the sky throughout the summer the direct illumination angle is reduced, which reduces the overall efficiency of the LSC.

3.7 Model Limitations

3.7.1 High Irradiance

Over the duration of the experiment (1 year), the flux incident on the Si cells has the potential to reach very low and very high intensities. Our model can accurately predict behaviour under very low and reasonably high illumination, however at intensities of over ten times one Sun (where one Sun $\approx 1000 \frac{\text{W}}{\text{m}^2}$), Auger recombination becomes the dominant form of recombination and continues to increase at a rapid rate, which is not accurately reflected in the current model.

3.7.2 Temperature

The temperature of the solar cell is assumed to remain constant at $T = 300 \text{ K}$. In the LSC case, unlike in direct PV, this is a more reasonable assumption as LSCs may be designed to inhibit transmission of infrared radiation, keeping the attached PV cool.

3.8 Analytical Model of Angular Reflection Losses

The front surface of the silicon cell used in our model is anisotropically etched to minimise reflection, with two layers of dielectric anti-reflection coatings deposited on top¹⁴. Hence, we have elected not to explicitly model the angle-dependant reflectivity of the Si cell when coupled to the LSC. All photons which make it to the LSC edge will be transmitted to the solar cell. However, we do model the silicon reflectance if no LSC is present.

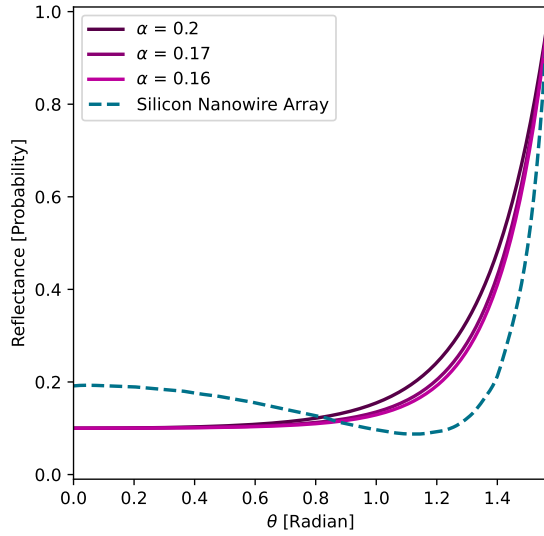


Fig. 21 Empirical model of silicon photovoltaic reflection losses utilised in the model (in purples) and a leading anti-reflection coating representing future reflectivity benefits in dashed blue.

Reflection losses in PV modules (AL) is performed by utilising an empirical analytical model^{22–24};

$$R(\theta) = R(0) + [1 - R(0)] \cdot \left[\frac{e^{-\cos(\theta)/\alpha} - e^{-1/\alpha}}{1 - e^{-1/\alpha}} \right] \quad (25)$$

where $\theta \in [0, \pi/2]$ is the angle of incidence and α the angular loss coefficient, a dimensionless parameter dependent on the PV system. α values range from 0.16 to 0.17 for commercial clean silicon and 0.20 if the modules' surfaces have a moderate quantity of dust^{22–24} (**SI Figure 21**). **Equation 25** is in good agreement with the experimental data and has been validated for all angles of incidence in a multitude of weather conditions^{22–24}. We use $\alpha = 0.17^{22}$ in the solar cell model with $R(0) = 0.1^{24}$, which represents PV with antireflection coatings.

Recent advances in anti-reflection coatings, including "black silicon" are remarkably close to the thermodynamic limit^{25–27}. Previously published surface reflectivity for s and p polarised light on a silicon nanowire array exhibits reduced reflection over the solar spectrum^{28,29}. The reflectivity of a surface may then be defined by

$$R(\theta, \phi) = R_s(\phi) \cos(\theta)^2 + R_p(\phi) \sin(\theta)^2, \quad (26)$$

where $R_s(\phi)$ is the coefficient of reflection for s-polarized light, $R_p(\phi)$ is the coefficient of reflection for p-polarized light, ϕ is the angle between the Poynting vector and the angle of incidence and θ is the angle between the electric field and the surface. For **SI Figure 21** we assume that $\cos(\theta)^2 = \sin(\theta)^2 = 0.5$. We observe that the small angle dependence may be

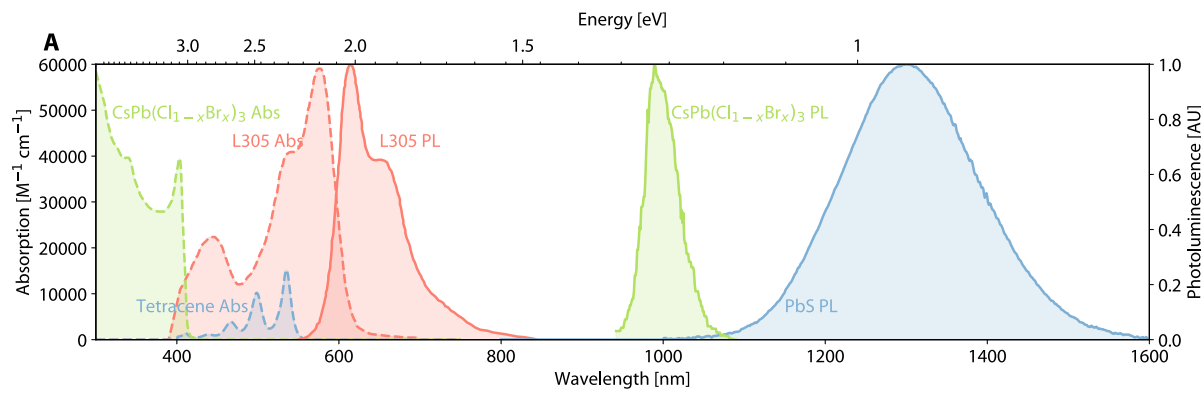


Fig. 22 A - Absorption (dashed line) and luminescence (solid line) of experimental demonstrations of singlet fission (in blue) and quantum cutting (in green) LSCs, along with a typical LSC dye (in red).

further improved relative to the empirical model in **SI Equation 25**.

4 Photomultiplier LSCs

4.1 Quantum Cutting

Demonstrations of QC LSCs (such as those depicted in **SI Figure 22**) which exhibit efficiencies of over 100% PLQE, consist of perovskite crystals doped with impurity ions^{30–32}. The 990 nm photoluminescence peak in **Figure 3A** in the main text corresponds to the $2F_{5/2}$ to $F_{7/2}$ f-f transition and low f-f oscillator strengths results in low reabsorption. It is supposed that the Yb^{3+} doping introduces defects in the perovskite crystal that rapidly localize excitation energy in the vicinity of the Yb^{3+} site. In or around this defect, the formation of the trapped excited state is followed by nearly resonant energy transfer to form two excited Yb^{3+} ions in a single quantum-cutting step, which results in the emission of two photons.

4.2 Singlet Fission

Singlet fission (SF) is an exciton multiplication process that occurs in organic semiconductors, where the initially photo-generated singlet exciton can convert to a triplet pair, which then breaks up to form two free triplet excitons³³. Demonstrations of singlet fission, such as the system depicted in **SI Figure 22** generate photoexcited triplets in tetracene which then diffuse until they encounter a PbS nanocrystal into which their energy can be transferred^{34–36}. Radiative recombination then occurs, with each triplet emitting a low-energy photon. The photons then may be directed by the LSC towards the solar cells at the edges, leave as a surface photon or be reabsorbed. SF has been demonstrated to enhance photocurrent in organic solar cells, organic/nanocrystal hybrid solar cells, as well as a parallel tandem silicon/pentacene solar cell^{37,38}. Singlet fission is known to be highly sensitive to molecular packing and the presence of the nanocrystal is known to disrupt the packing of the molecules over which the singlet fission takes place^{35,36,39}. From observation of the nanocrystal photoluminescence in the experimentally demonstrated singlet fission system, it is obvious that the majority of the emitted photons are beyond the bandgap of the silicon solar cell, inhibiting the effectiveness of the Tet-PbS LSC (see **SI Figure 22**). This highlights that the quantum dot must be engineered such that acceptor states lie below the triplet energy, thus facilitating efficient triplet energy transfer, yet above the silicon bandgap. This remains a challenge in experimentally

demonstrated systems. The concentration of the emitting nanocrystal may be very low relative to the absorbing species (tetracene), such that may be neglected

5 LSC Size Considerations

Here we attempt to analytically determine the best possible size of an LSC within the context of coupling LSCs to solar cells. We consider the LSC geometry to be limited on two fronts:

1. The concentration dependent recombination pathways within the solar cell, and
2. Photon loss pathways that also impose diminishing returns on solar flux as a function of size. These may include:
 - (a) Substrate Reabsorption
 - (b) Chromophore Reabsorption & Surface Losses

Thus, will be some optimum balancing the two factors. Photon loss pathways are a function of the photon pathlength in the LSC, whereas recombination pathways within the solar cell is a function of the output photon flux of the LSC, which itself is a function of the input photon flux and photon loss pathways.

5.1 Losses as a function of photon pathlength

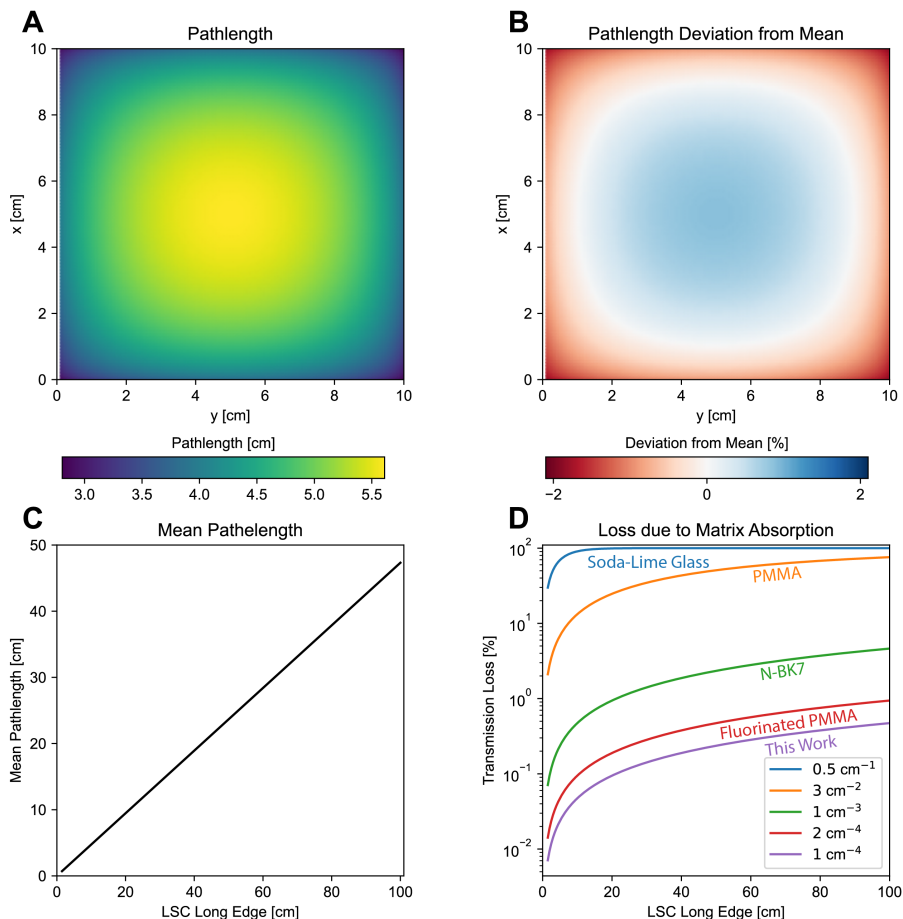


Fig. 23 A - Gives the average pathlength to an accepting edge for an emitting chromophore exhibiting anisotropic emission in the 10 by 10 cm LSCs described in the main text. B - Plots the percentage deviation from the mean value for the 10 by 10 cm LSC which is 4.73 cm. Photons hitting the corners and the centre of the LSC must travel furthest. C - Plots mean pathlength as a function of LSC size, assuming the square LSC design. D - Transmission losses due to LSC matrix as a function of LSC size, using the mean photon pathlength assumption.

Photon losses as a function of pathlength can be experimentally determined¹ or determined using montecarlo algorithms. However, in the assumption of a LSC that exhibiting anisotropic emission as well as negligible reabsorption from the chromophore (e.g. the quantum dot LSC), the average photon pathlength will approach, \bar{l} . We define the average path length as the average distance a photon will travel from the illumination point to the photon accepting edges. Note, that this assumption makes an implicit distinction from actual photon pathlength in LSC, which is often recovered from a ray-tracing simulation, which will account for the real distance a photon travels due to reflection events (as in **SI Figure 13**).

The average photon pathlength can be determined analytically. Let (p_x, p_y) define the illumination point and L represent the length of one edge of the LSC. In polar coordinates, the integral is the length of the paths along the angle of acceptance, divided by the angle of acceptance, doing so we can recover an analytical expression for the average path length.

$$\begin{aligned} \bar{l} &= \frac{\int_{\theta_{\min}}^{\theta_{\max}} d(\theta) d\theta}{\int_{\theta_{\min}}^{\theta_{\max}} 1 d\theta} = \frac{\int_0^1 d(y) \frac{d\theta}{dy} dy}{\int_0^1 \frac{d\theta}{dy} dy} \\ &= \frac{\int_0^L \sqrt{p_x^2 + (y - p_y)^2} \frac{d}{dy} (\tan^{-1} [p_x, y - p_y]) dy}{\int_0^L \frac{d}{dy} (\tan^{-1} [p_x, y - p_y]) dy}, \end{aligned} \quad (27)$$

where \tan^{-1} is the two argument arc tangent. This can be analytically solved for arbitrary $L > 0$ as

$$\bar{l}(p_x, p_y) = \frac{p_x \left(-\log \left(\left(\sqrt{p_x^2 + p_y^2} - p_y \right) \left(\sqrt{(L - p_y)^2 + p_x^2} - L + p_y \right) \right) + \log \left(\sqrt{(L - p_y)^2 + p_x^2} + L - p_y \right) + \log \left(\sqrt{p_x^2 + p_y^2} + p_y \right) \right)}{2 \left(\tan^{-1} \left(\frac{L - p_y}{p_x} \right) + \tan^{-1} \left(\frac{p_y}{p_x} \right) \right)}.$$

The photon pathlength for each point $= (p_x, p_y)$ when each LSC edge is accepting photons is then

$$\bar{l}(p_x, p_y) + \bar{l}(p_y, p_x) + \bar{l}(p_y, p_x - L) + \bar{l}(p_x, p_y - L), \quad (28)$$

which is possible because of the symmetry of the solution in the square LSC. The solution for a 10 cm by 10 cm LSC is plotted in **SI Figure 23**. The average pathlength over the entire LSC is the double integral of $\bar{l}(p_x, p_y)$ from 0 to L , divided by $2L$, which for $L = 10$ cm is equal to 4.73 cm;

$$\frac{1}{L^2} \int_0^L \int_0^L \bar{l}(p_x, p_y) + \bar{l}(p_y, p_x) + \bar{l}(p_y, p_x - L) + \bar{l}(p_x, p_y - L) dp_x dp_y = 4.73 \text{ cm} \quad (29)$$

SI Figure 23A plots $\bar{l}(p_x, p_y)$ and **SI Figure 23B** plots the deviation from the mean, we see that there is no greater than $\approx 2\%$ deviation from the mean value of \bar{l} across the LSC so we use the mean value for determination of absorption losses. **SI Figure 23C** plots the linear relationship between LSC and mean pathlength over the LSC and **SI Figure 23D** plots the average loss the LSC would suffer from matrix absorption for the substrates given in **Table 1** in the main text.

5.2 Solar cell recombination limitations

Cell	Source	V_{OC} [V]	J_{SC} [mA/cm ²]	FF [%]	η [%]	R_s [Ω/cm^2]	R_{Sh} [Ω/cm^2]	J_{NR} [pA/cm ²]	l [μm]
1	40	0.648	36.29	75.7	17.8	1.48	1800	400	170
2	41	0.638	37.19	76.7	18.2	1.15	1300	591	180
3	42	0.65	37.38	76.2	18.5	1.35	1800	386	180
4	43	0.649	37.5	78.9	19.2	0.82	1800	400	190
5	44	0.692	36.41	77.4	19.5	1.28	1200	72	180
6	45	0.657	38.1	79.5	19.9	0.73	2000	297	180
7	46	0.663	39.03	80.3	20.8	0.59	2000	241	190
8	47	0.674	41.07	80.5	22.3	0.6	3000	166	195
9	44	0.742	39.31	81.6	23.8	0.67	2000	10	150
10	45	0.736	41.39	80.1	24.4	0.75	800	13	200
11	48	0.74	41.81	82.7	25.6	0.47	4000	12	150
12	45	0.744	42.26	83.8	26.4	0.31	6000	10	200
13	49	0.738	42.65	84.9	26.7	0.08	10000	13	200

Table 1 Outlines parameters used within the model to produce SI Figure 24. Cell 13 was used throughout study unless explicitly otherwise mentioned.

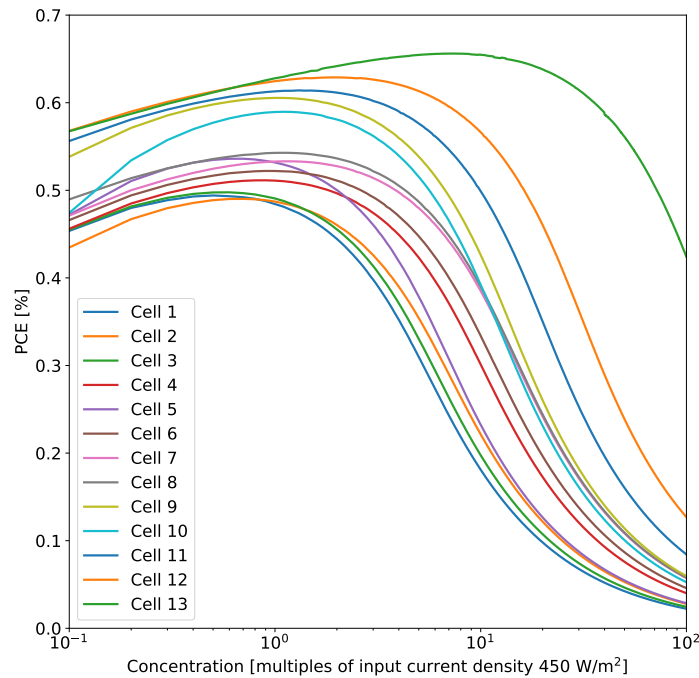


Fig. 24 Modelled PCE loss as a function of increasing concentration.

SI Figure 24 outlines the effect of concentration on the PCE on silicon solar cells (see details of solar cells in **SI Table 1**). For the PCE calculation at concentration = 1, the power input is given as 450 W/m², which acts as an approximation for the equivalent power for absorbed photons at AM1.5 conditions for silicon photovoltaics. For low concentration factors ($\sim 1 - 10$) the increased photon flux results in an increased PCE. However, beyond concentration factors of ≈ 10 the PCE dramatically drops for all cells apart from the Cell 13, which was chosen for this study as PCE increases until $C \approx 15$). For all solar cells, this decrease in PCE as a function of concentration sets an upper limit to the useful concentration of an LSC, which will be pinned by the solar cell used. This may be understood predominantly in terms of Auger recombination, which scales exponentially - $\propto x^3$ - see **Equation 2** in the main text. **SI Figure 25** plots different loss mechanisms for

different input current densities.

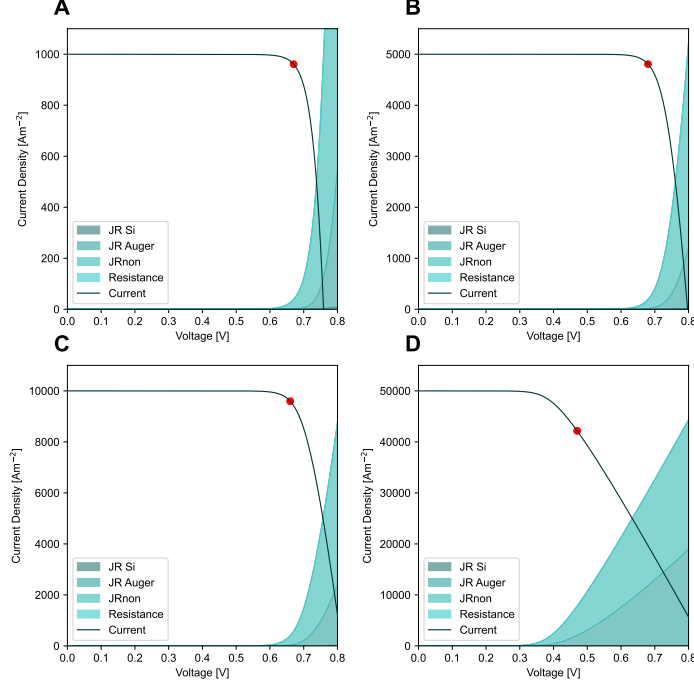


Fig. 25 Simulated JV curves with varying concentration based on illumination in Amsterdam on Wednesday 17th July 2019 at noon in Amsterdam.

5.3 Recombination limits in the Real World

To determine the maximum LSC size in real world conditions, we use diffuse and direct illumination intensities from Baseline Surface Radiation Network (BSRN)^{50–59}. To investigate the flux dependent recombination in general terms, we apply a toy model, which is distinct from the raytracing simulations used in the main text. We assume all photons that fall within the EQE of the solar cell may be absorbed, and the concentration factor simply acts to increase this flux. This allows us to ignore the LSC losses which do not scale linearly with size, for example, a larger or thicker LSC will have a different photon path length. We took the mean of 10 thousand minutes or roughly 160 hours (effectively 1 week) of the highest recorded intensities as the maximum intensity for each location, ϕ_{input} . We note that by taking the mean of highest intensities over such a long time period may also be poor approximation for the illumination intensity to optimise to in these locations, but in all cases gives a useful upper bound. Assuming standard solar illumination, the radiation that was possible for Cell 13 (see **SI Figure 24**) to absorb is calculated by

$$\phi_{\text{abs}} = \int_{280}^{1000} \text{CF EQE}(\lambda) \text{AM1.5}(\lambda) d\lambda \quad (30)$$

where CF is a correction factor given by,

$$\int_{280}^{4000} \text{AM1.5}(\lambda) \text{ CF } d\lambda = \phi_{\text{input}}. \quad (31)$$

SI Table 2 summarises these results. **SI Figure 26** depicts some of the difference in the terrestrial spectral environment for these locations.

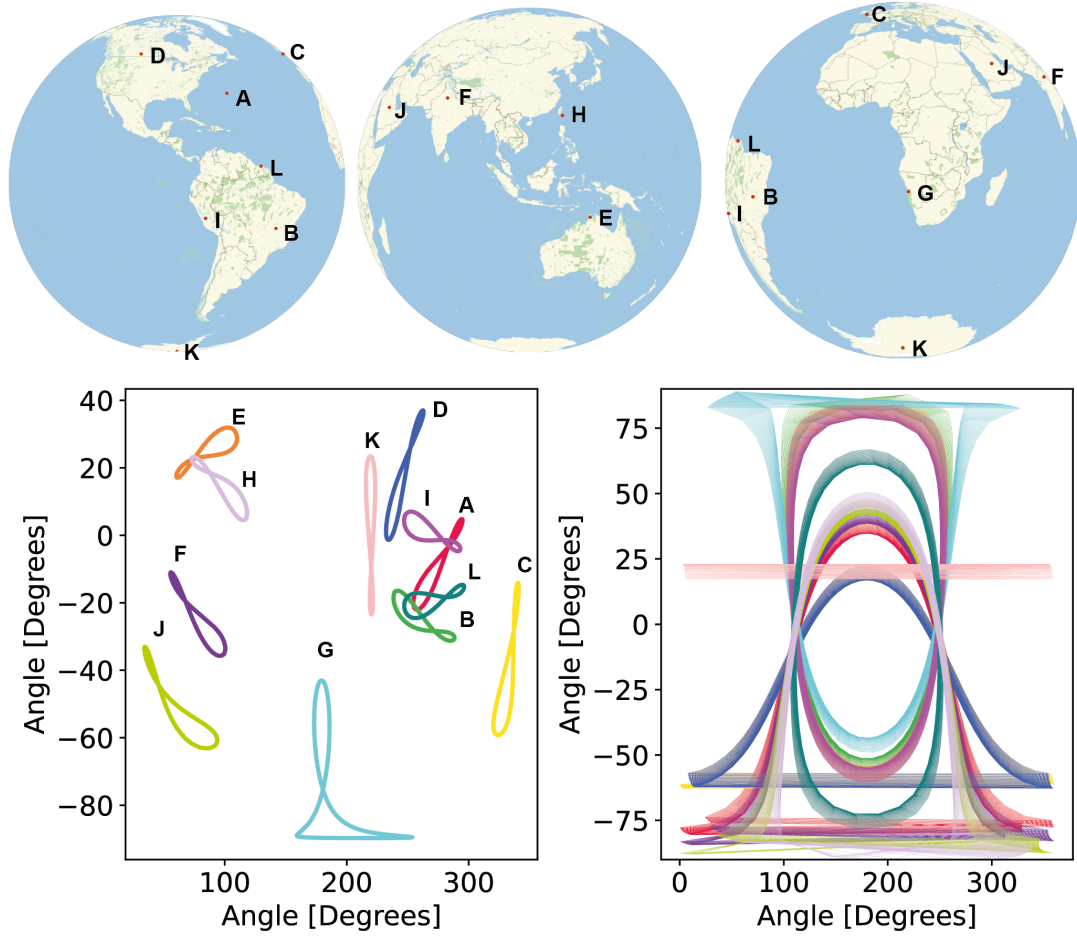


Fig. 26 Top – Geographical locations of metrological sites, covering every continent and both hemispheres. Left – Solar analemma over the calendar year 2022 at midnight UTC, demonstrating that these locations represent solar spectra over a wide array of latitudes and longitudes and hence differing direct illumination profiles. Right – Sun position for each location from January to February 2022, where values above 0 are above the horizon.

Measurement [W/m ²]	BER	BRB	CAM	REG	DAR	GAN	GOB
$\phi_{\text{input, direct}}$	918.191	972.844	957.362	958.402	928.617	764.77	1036.53
$\phi_{\text{input, diffuse}}$	490.302	541.063	239.648	479.432	530.77	517.027	451.868
$\phi_{\text{abs, direct}}$	662.099	701.509	690.345	691.095	669.617	551.469	747.4316
$\phi_{\text{input, diffuse}}$	353.553	390.156	172.808	345.714	382.733	372.824	325.838
Measurement [W/m ²]	MNM	OHY	SOV	SPO	PAR	LYU	
$\phi_{\text{input, direct}}$	925.476	1041.96	1027.25	1044.7	879.498	889.703	
$\phi_{\text{input, diffuse}}$	488.336	589.175	462.569	366.235	556.9	587.36	
$\phi_{\text{abs, direct}}$	667.353	751.35	740.741	753.325	634.198	641.556	
$\phi_{\text{input, diffuse}}$	352.135	424.849	333.554	264.089	401.575	423.54	

Table 2 Outlines parameters used for SI Figure 36.

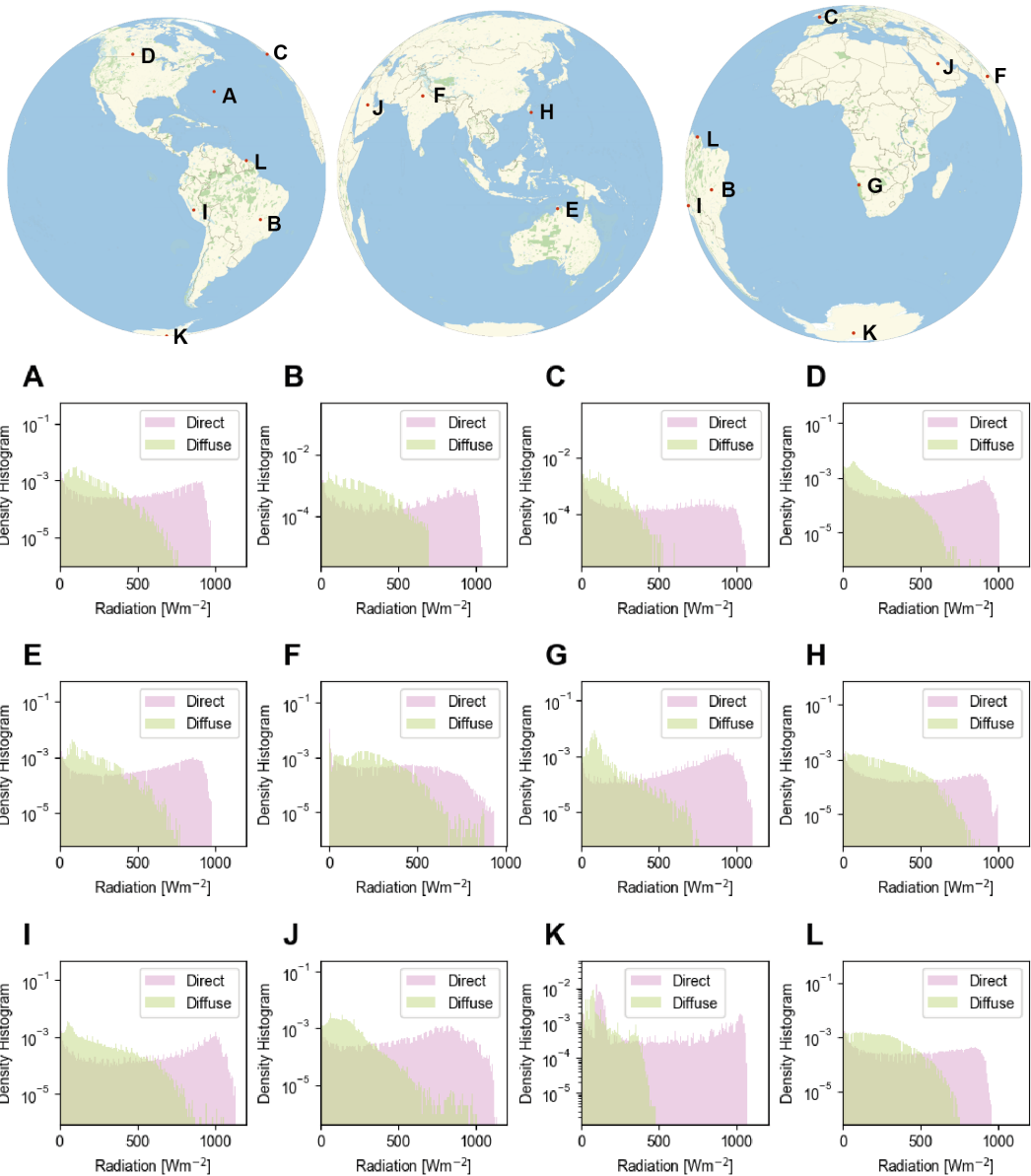


Fig. 27 – A - L Labels correspond to the locations of metrological measurement sites as in Referee Response Figure 1 (Top). The locations represent differing distribution of direct (in pink) and diffuse illumination (in green). Histogram represents the probability density (i.e. the histogram sums to 1) of finding a one minute interval at each radiation intensity, including times where no illumination is recorded (i.e. radiation = 0), which is not plotted.

6 Results

6.1 Streamgraphs

We detail streamgraphs that pictorially represent the photon pathways within the simulation. Streamgraphs start with a set number of photons considered by the simulation. Curves and widths of boxes that follow are directly proportional to the number of photons that travel that route within the simulation. A curve may be thicker than the initial number of input photons, as a photon may undergo multiple photon reflection, transmission and absorption events. However, the total of the final destinations of the photons matches the input photon number other than in the LSCs where photon multiplication is active. Within the portions of the streamgraph that consider electrical losses these are proportionally scaled to photon

number to photons absorbed by the solar cell.

6.1.1 Ray-tracing Streamgraph

Two LSC simulations are depicted for the ray-tracing simulation. Firstly the photon paths within the dot-directional LSC is given in **SI Figure 28**. Similarly for the Lumogen LSC, the equivalent figure is given in **SI Figure 29**. For each LSC, two streamgraphs are given, the first which displays the path of ten thousand blue photons at impinging 10 degrees at then the same number impinging at 90 degrees. Photon loss is defined as any photon which leaves the simulation region, this may be due to reflection or due to an absorption then surface loss.

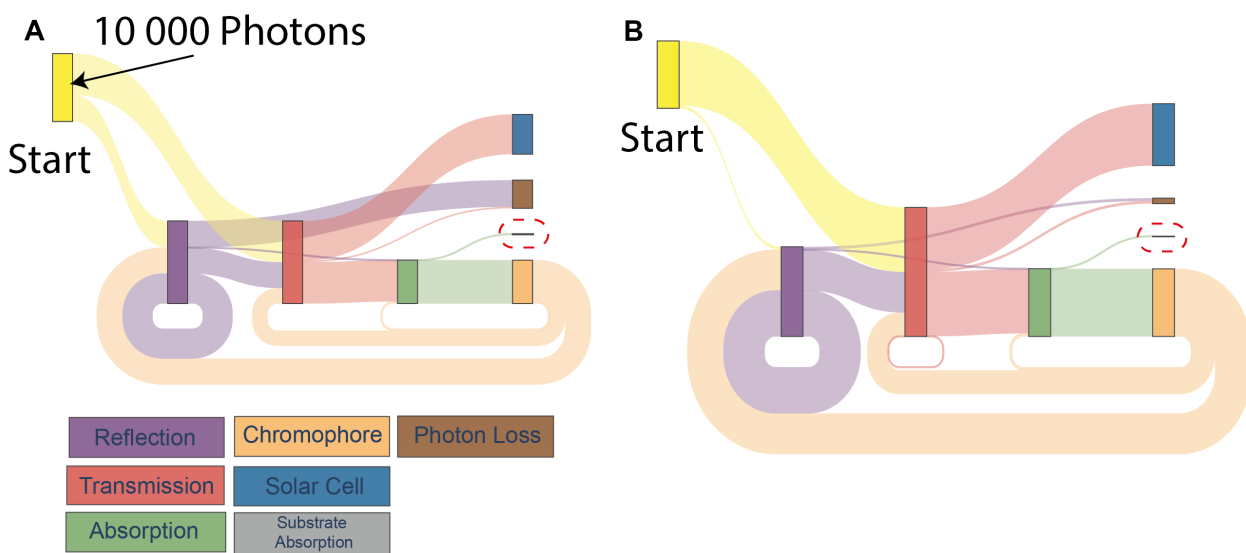


Fig. 28 Each simulation starts with 10000 photons (at the start location, in yellow). The thickness of the curves corresponds to the path each photon takes. Note, that a photon may go through a specific operation more than once. The red dotted line highlights substrate absorption. Photon loss occurs when a photon leaves the simulation area. A – corresponds to 10k blue photons impinging the LSC at 10 degrees and B – corresponds to 10k blue photons impinging the LSC at 90 degrees.

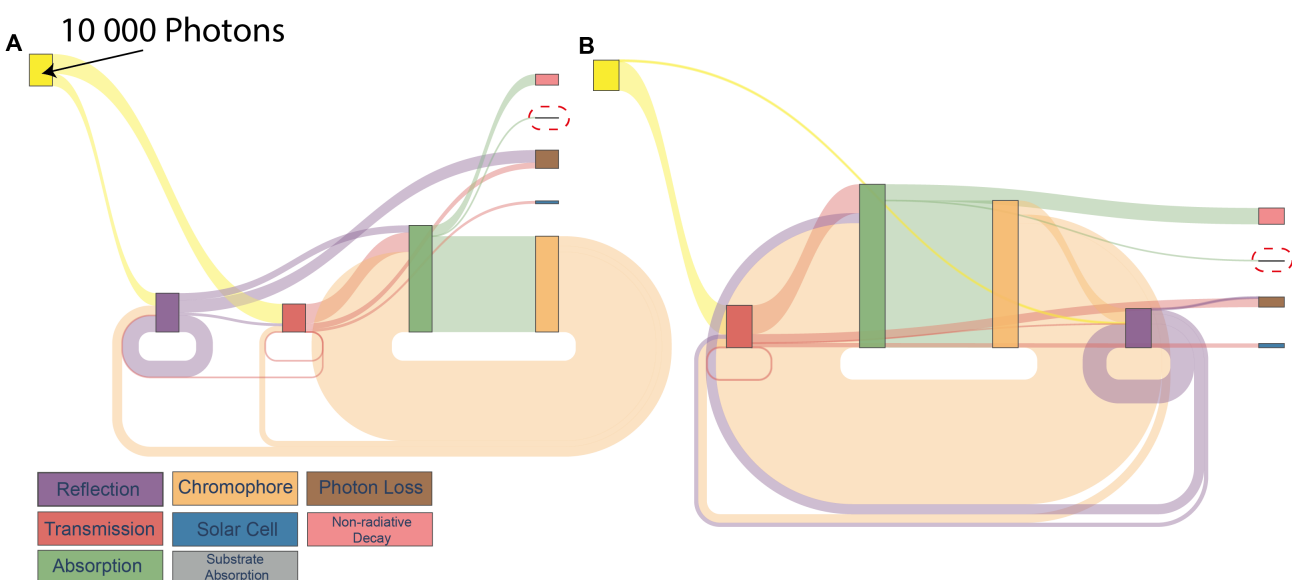


Fig. 29 Each simulation starts with 10000 photons (at the start location, in yellow). The thickness of the curves corresponds to the path each photon takes. Note, that a photon may go through a specific operation more than once. The red dotted line highlights substrate absorption. Photon loss occurs when a photon leaves the simulation area. A – corresponds to 10k blue photons impinging the LSC at 10 degrees and B – corresponds to 10k blue photons impinging the LSC at 90 degrees.

6.1.2 Complete Simulation Streamgraph

The streamgraphs outlining the complete simulation, from including both the photon angles impinging, raytracing and electrical losses, are given for the combined directional LSC **SI Figure 30** and for the Lumogen LSC in **SI Figure 31**. Again, the photon paths and the widths of the boxes are proportional to the number of photons that travel through that route. The input photons, depicted by yellow boxes, represent that photons that impinge on the LSC at noon and the following 15 minutes on the 7th of July 2019 on the LAD detector in AMOLF. These photons are described by the angle they impinge the detector (blue boxes), and their wavelength (purple boxes).

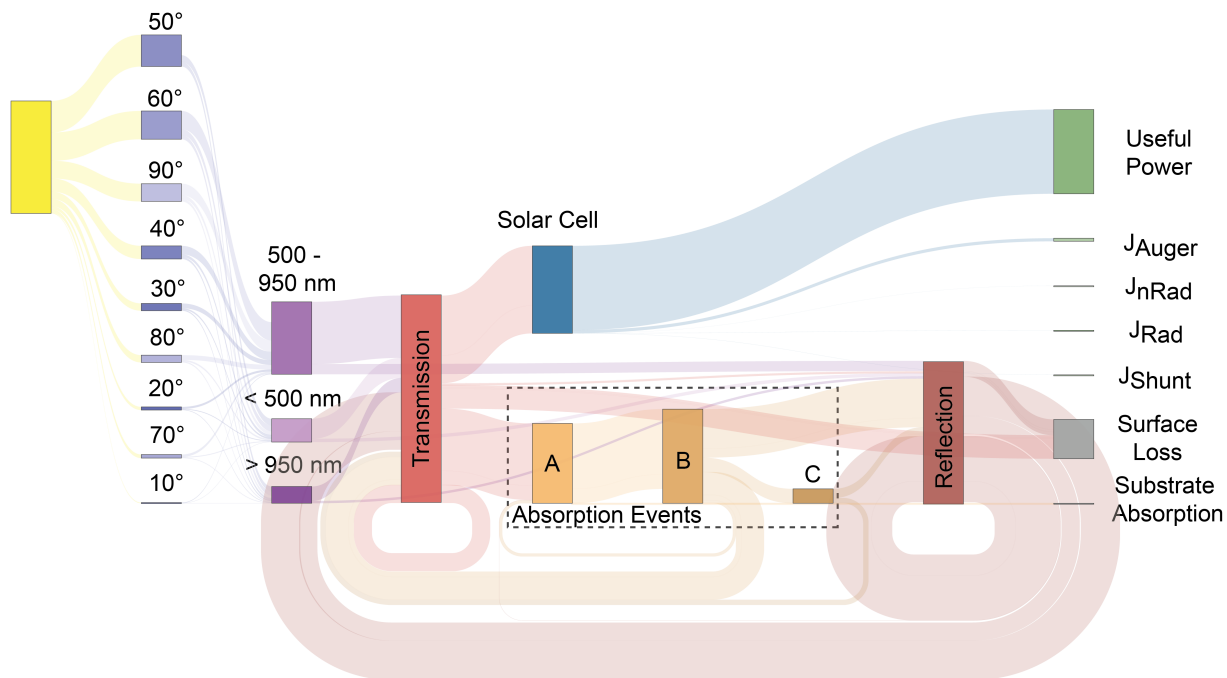


Fig. 30 Pathways in the Combined Directional LSC. Yellow box indicates photons that impinge the LSC in a 15 minute interval on the 7th of July 2019 at noon in Amsterdam. All box heights and pathways are to scale to these initial photons. The spectrum is angle resolved, here plotted in 10-degree segments that impinge on the LSC. Of interest in the Lumogen LSC are photons that may be absorbed (< 450 - 650 nm) and those which are transmitted by the LSC. A photon may undergo multiple transmission events before it impinges on the LSC. A dashed box depicts photon/matter interactions beyond reflection and transmission. Box A gives the number of photons absorbed by the chromophores within the LSC. Box B depicts emission, which is slightly larger than box A due to the fact the chromophores may undergo a photon multiplication process, resulting in two photons for one photon absorbed. Box C depicts those photons whose origin is photon multiplication. If the photon travels to the solar cell, in blue, it may either contribute to useful power, or decay in an electronic loss current, such as Auger, non-radiative recombination (nRad), radiative recombination (Rad), or through resistance (JShunt). Surface loss refers to photons that are optically lost to the LSC and leave the simulation region.

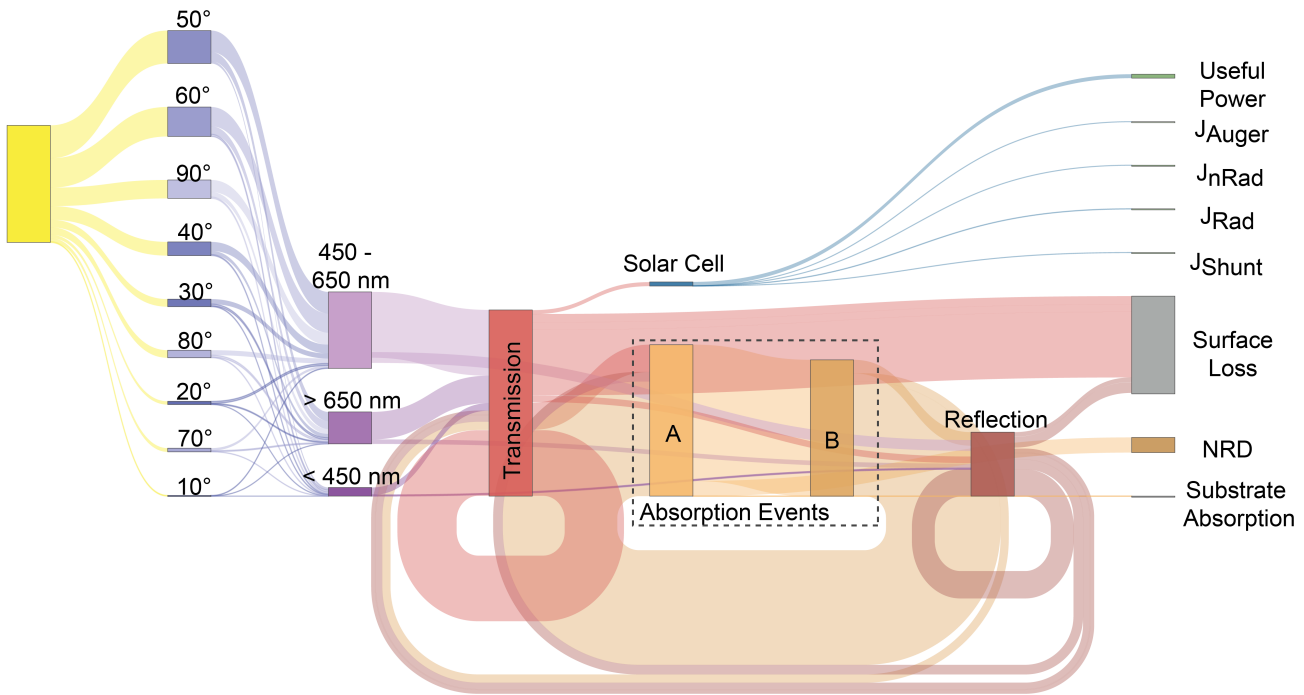


Fig. 31 Referee Response Figure X – Loss pathways in Lumogen LSC. Yellow box indicates photons that impinge the LSC in a 15 minute interval on the 7th of July 2019 at noon in Amsterdam. Box A is an absorption event, where photons may either to substrate absorption (a loss pathway) or chromophore absorption with some quantum efficiency, or decay nonradiatively, (NRD). All other definitions the same as SI Figure 30.

6.2 Expanded Geographical Locations

Using published solar irradiance data^{50–59}, **SI Figure 26** depicts the combined directional LSC modelled in every continent over the course of a few days. Locations cover both hemispheres and a broad selection of latitudes and longitudes. These locations fairly represent a broad range of differing distributions of direct and diffuse illumination.

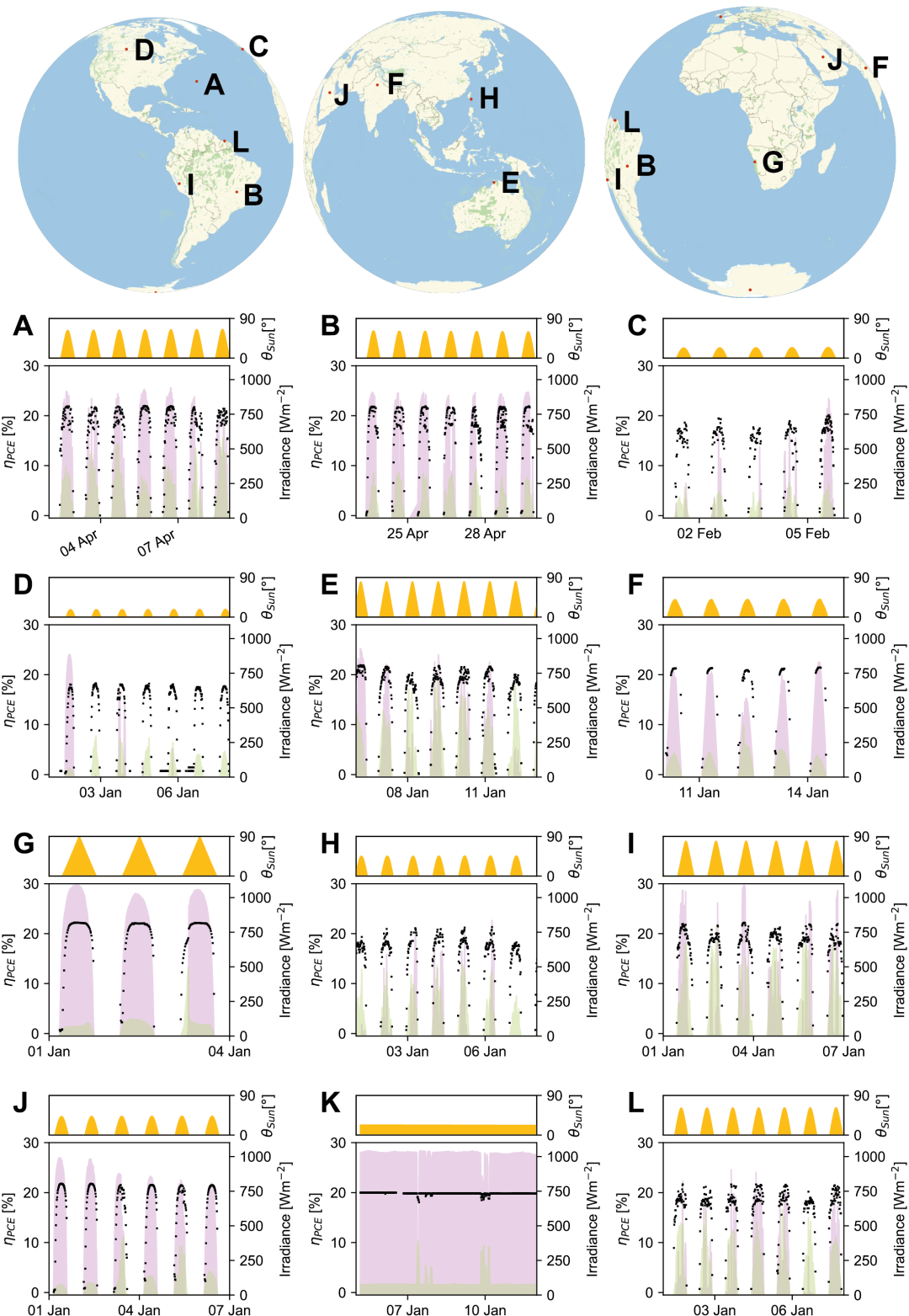


Fig. 32 A - L Labels correspond to the locations of metrological measurement sites as in SI Table 1. The locations represent differing distribution of direct (in pink) and diffuse illumination (in green). Histogram represents the probability density (i.e. the histogram sums to 1) of finding a one minute interval at each radiation intensity, including times where no illumination is recorded (i.e. radiation = 0), which is not plotted.

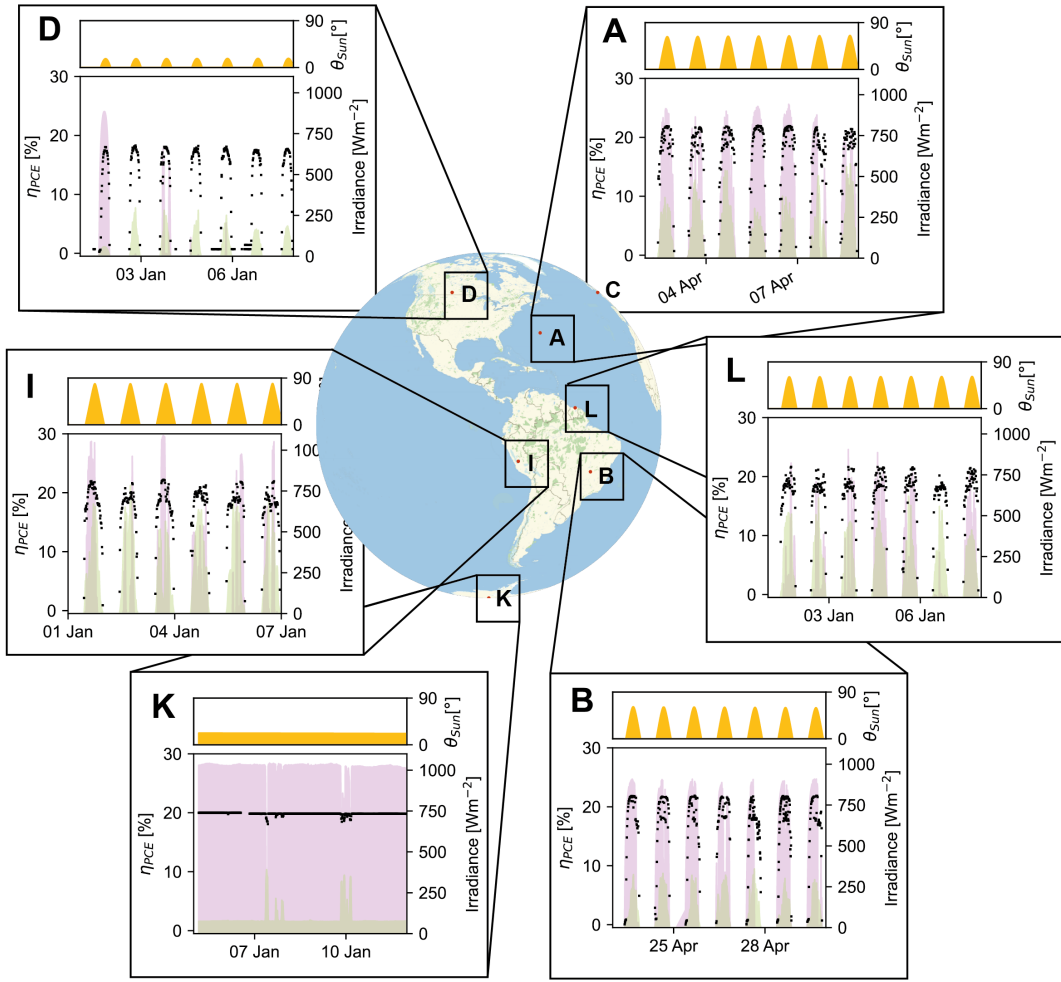


Fig. 33 A - L Labels correspond to the locations of metrological measurement sites as in SI Figure 32. For each location, a week is plotted on the x axis. Black points give the η_{PCE} of the combined direction LSC device described in the main text. Superimposed is the time resolved irradiance of direct (in pink) and diffuse illumination (in green). Above, in yellow, is the angle direct illumination makes with the horizontal LSC. All times are UTC and in K, the sun never sets due to the southern polar summer.

6.3 Diffuse and Direct Comparison

Here we compare the utilisation of LSCs in diffuse environments, specifically, comparing LSCs to optical concentration systems in **SI Section 6.3.1** and to silicon PV in **SI Section 6.3.2**.

6.3.1 Comparison to Optical Concentration

Here we consider the purported advantages of LSCs in diffuse and direct illumination. Direct normal irradiance (DNI) excludes diffuse solar radiation (radiation that is scattered or reflected by atmospheric components). Diffuse horizontal irradiance (DHI) is typically reported as a radial integral of spectral intensity from all other angles. DNI is typically measured only for the upper hemisphere of measurement. Using our homebuilt Light Ambient Detector (see **SI Section 1**), we are able to relax these constraints and use the full angular resolved diffuse spectrum, indeed, the distinction between DNI and DHI is largely arbitrary in this context.

DNI can be corrected for to consider horizontal alignment conditions by multiplying the spectra times the zenith angle, the dataset we term DNI_ϕ (calculated here by $\text{DNI}_\phi = \text{GHI} - \text{DHI}$). We can now compare DNI_ϕ with DHI, which is given in

SI Figure 34. A solar concentrator that can accept both direct and diffuse light will always be optimal, but **SI Figure 34** delineates where diffusely accepting concentrators will always out compete to traditional optical concentrators.

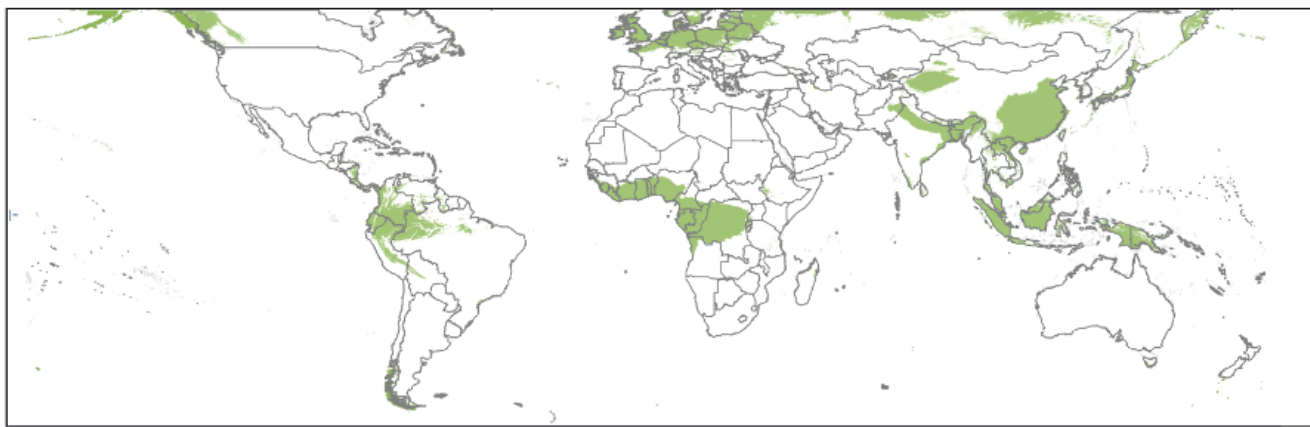


Fig. 34 Green regions represent regions where diffuse irradiation is greater than direct illumination, where the concentrating device is held flat.

6.3.2 Comparison to Silicon

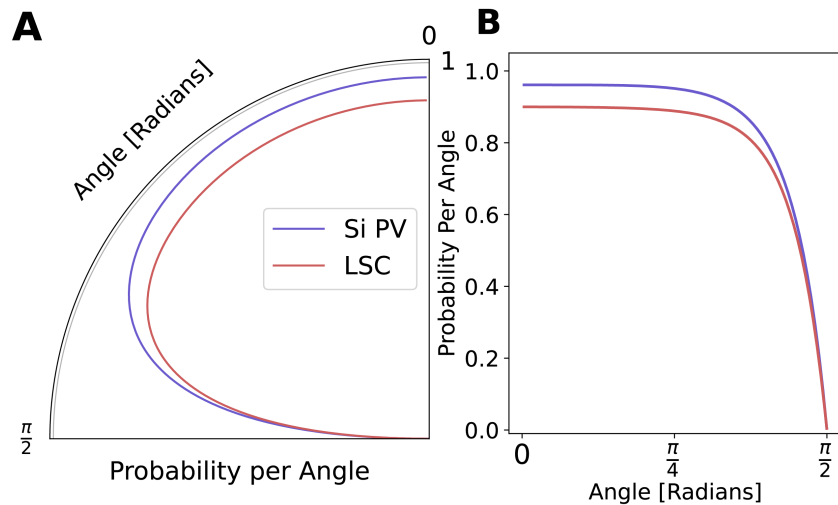


Fig. 35 Probability distribution functions (PDF) for transmission where 0 degrees is normal to the device. Red line represents a LSC matrix described and Si PV described in the main text. A and B plot identical data.

In **SI Figure 35** we consider the probability density function (PDF) for reflection for a matrix as described in the main text (see **Main Text Table 1**) and the Si PV described in **SI Section 3.8**. We find at all angles the Si PV may absorb more strongly than the silicon cell, this might be expected as refractive index primarily defines reflection, and silicon's $n_{\text{Si}} \approx 4$ is greater than all reported LSC refractive indices (see **Main Text Table 1**). There is no diffuse or direct irradiance ratio where the LSC will accept more photons relative to Si PV.

Importantly the advantage that the LSC offers is not that the LSC can accept inherently more diffuse radiation per unit area, but that the concentration factor can be improved to match the optimum of the cell. The primary advantage of LSCs in the context of energy capture will be the niche where LSC concentration reduces the requirement for more solar cells, but before auger combination kicks in (which is a function of photon flux and hence concentration factor of the LSC). **SI Figure 36** plots this for various locations on the planet. We observe, in these limiting cases that even in diffuse

environments, moving much beyond 10 cm square LSCs, offers disadvantage to the solar cell and much energy is lost in Auger recombination. Of course, if the LSC has a poor optical efficiency then the LSC may be bigger than described here.

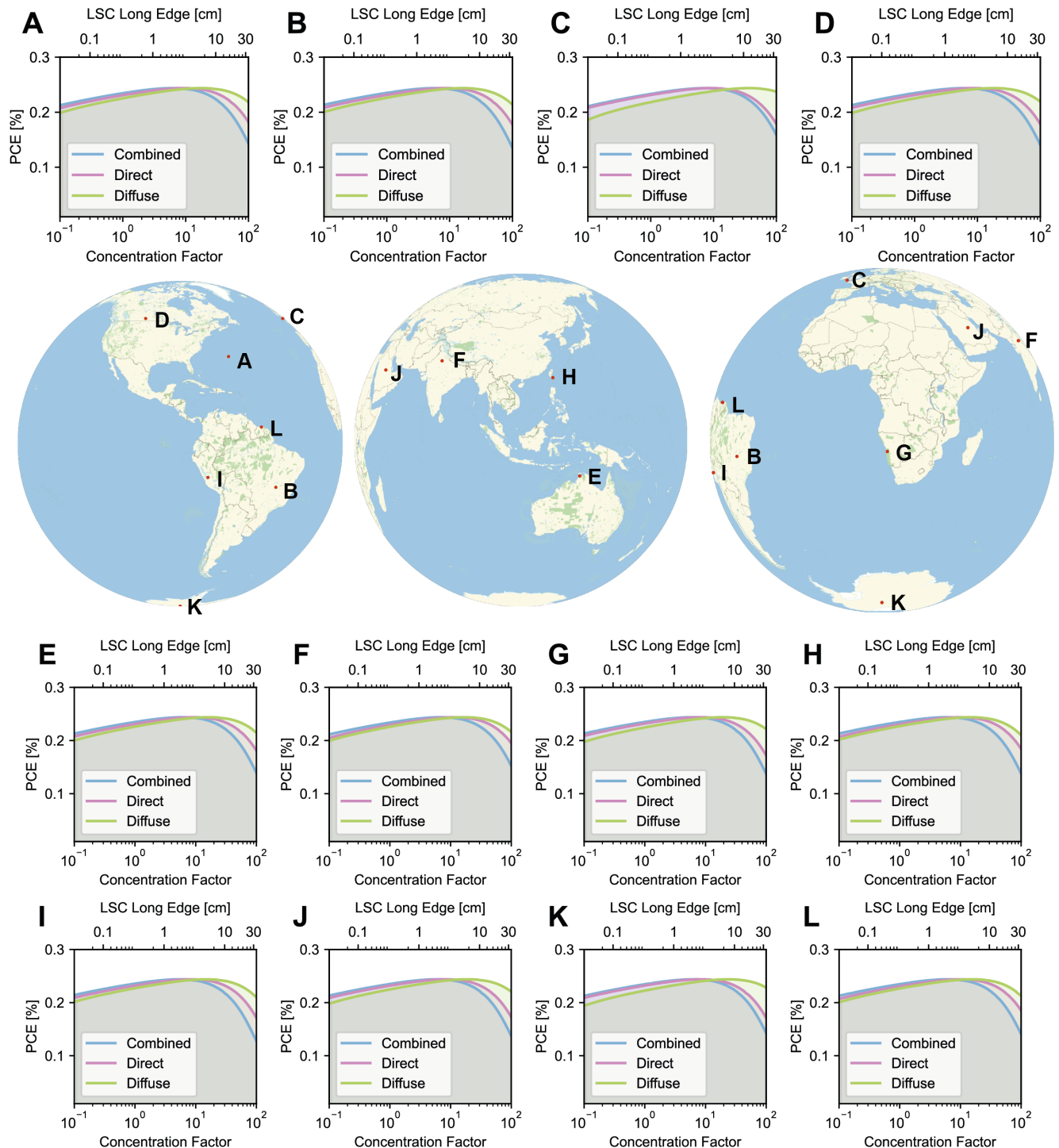


Fig. 36 Concentration dependent η_{PCE} for locations around the world. The green line considers just direct illumination, the purple line just direct and the blue line is the flux sum of both. The magnitude of the input fluxes are specified in SI Table 2. The simulation assumes losses concentration.

6.4 Bifacial LSCs

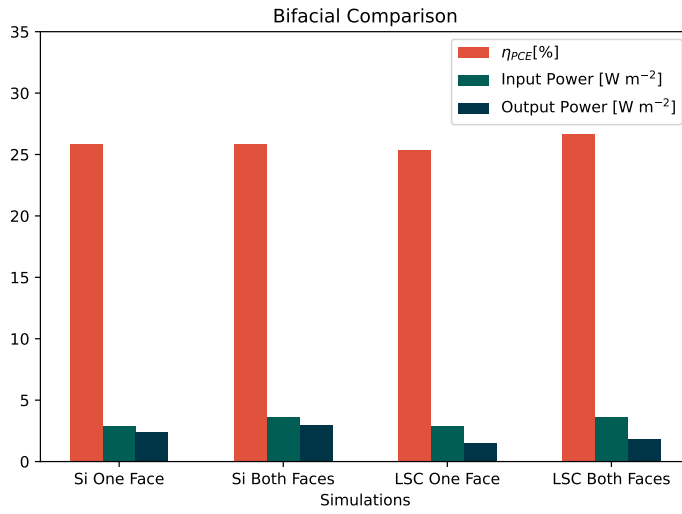


Fig. 37 Power conversion efficiency, input power and output power measured over a 15 minute interval on Wednesday the 17th July 2019 at noon for the Combined Directional LSC.

There remain unresolved research questions in bifacial solar cells that remain beyond the scope of this paper and inhibit us from definitively stating that LSCs may/may not outperform bifacial PV, primarily concerning current matching requirements⁶⁰. These current matching requirements are not implemented within in our circuit model. Therefore, we make no general conclusion on the advantages of LSCs relative to bifacial cells. However, it is readily possible to outline the results for specific configurations: (1) An Si PV pointing upwards; (2) Si PV simultaneously pointing upwards and downwards; (3) An LSC PV accepting only light impinging from the top surface and (4) LSC PV accepting both.

In our Amsterdam detector - where we have reasonable data from below the horizon - due to the raised placement of the sensing array . Therefore, the modelled LSCs based on LAD can readily include contribution from the bottom. This is not immediately possible (or only with some reflection assumptions, although the albedo for many surfaces is well known) in Colorado, since these detectors are unhelpfully mounted on an opaque roof. As such we have run the simulations and outline the results below, in **SI Figure 37**, where we find that the bifacial LSC efficiency increases when the inclusion of back and front irradiation.

6.5 LSC Thicknesses

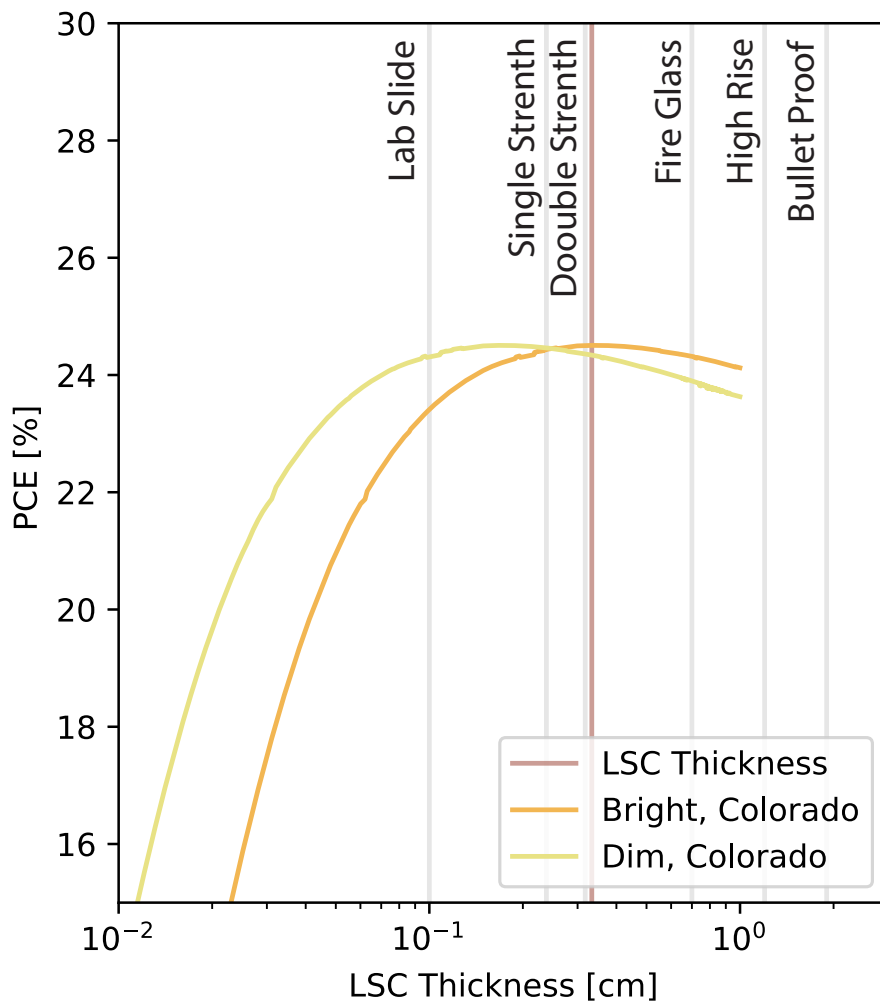


Fig. 38 LSC thicknesses, which impacts the concentration factor for the Combined Directional LSC in Colorado. Overlaid in red is the LSC thickness and other labelled thicknesses in grey.

Within the simulation, users may choose any thicknesses appropriate for their application. The vast majority of residential windows use Double Strength glass which is defined as $1/8$ " thick, very close to the $1/3$ cm value. This value was chosen rationally based on the reasonableness of the concentration factor.

6.6 Other LSC Use Cases

LSCs have reported applications in reaction chemistry^{61–69}, greenhouses^{65,70–72}, optical communication⁷³, solar pumped lasers⁶¹. For these applications, the photon flux is important. SI Figure 39 plots the simulated photon efficiency of the LSC as a function of input angle and input wavelength. Photon efficiency is defined by the number of photons incident on the LSC relative to the number which are emitted by the edges of the LSC. Photon efficiency should not be confused with internal efficiency η_{int} , which is a measure of the absorbed photons. Therefore photon efficiency also accounts for refraction of unabsorbed photons through the LSC, as can be observed in SI Figure 40 over wavelength regions where the input wavelength is equal to the output wavelength and where the input wavelength but not absorbed by the LSC.

Further, note that the emission is not a perfect Gaussian due in the quantum dot LSCs due to the fact that some emission wavelengths are within the absorption of the dot LSC, meaning the Gaussian is clipped at 950 nm.

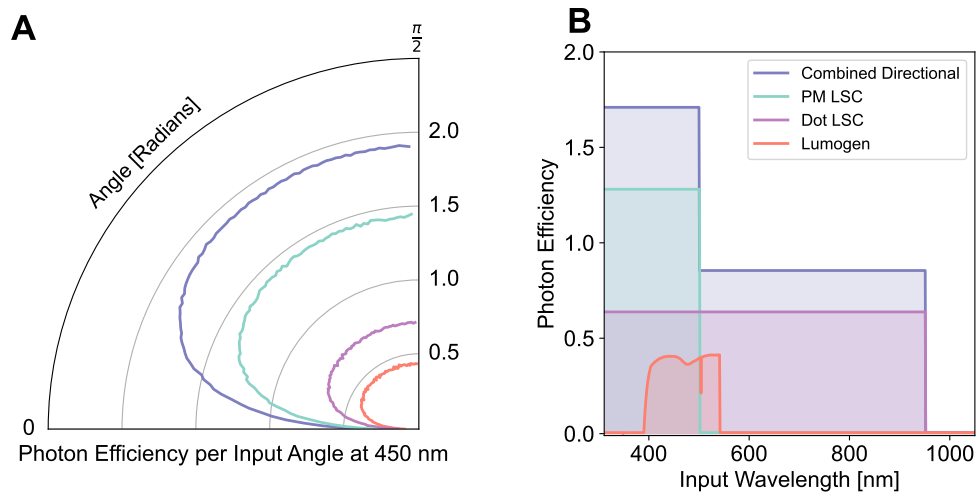


Fig. 39 A - Plots the angle dependent ray tracing results between 0 and $\pi/2$ radians for the 10 cm^2 described in the text where the photons impinging at 450 nm, where $\pi/2$ represents photons impinging onto the LSC. B - Photon efficiency as a function of input wavelength, for different LSC designs. Photon efficiency is defined as all the photons which are incident on the LSC divided by the photons which are emitted from the edge.

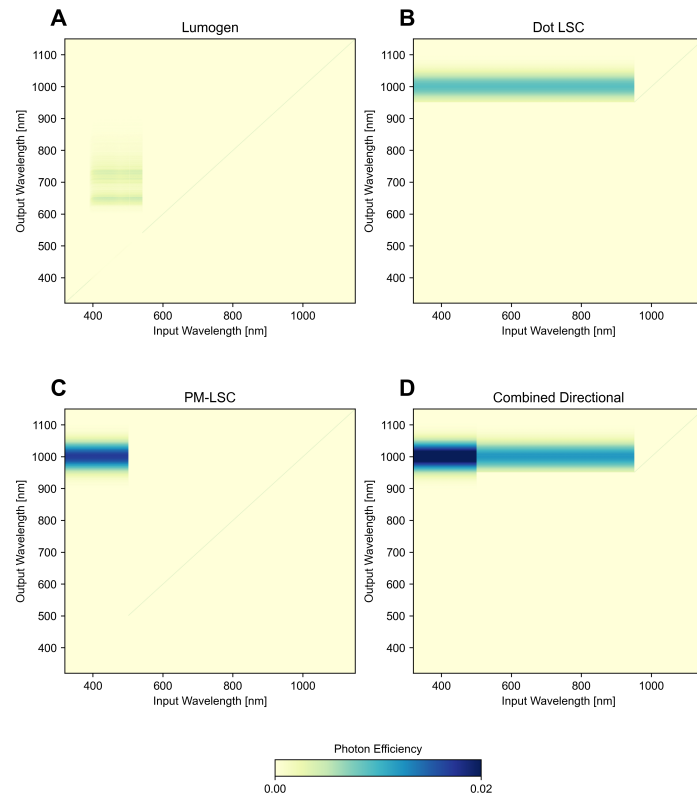


Fig. 40 Photon efficiency maps as a function of input and output wavelength for the 10 cm^2 LSC described in the text. A - Lumogen LSC which exhibits an absorption and emission overlap, B - Dot LSC exhibiting broad absorbance, C - PM LSC with 200% chromophore PLQE below 450 nm, and D - the combined PM-dot LSC with directional emission. Absorbance and PL are as described in Figure 3. Note, the efficiency of refraction through the LSC is visible over output wavelengths match the input wavelength in regions of negligible LSC absorption.

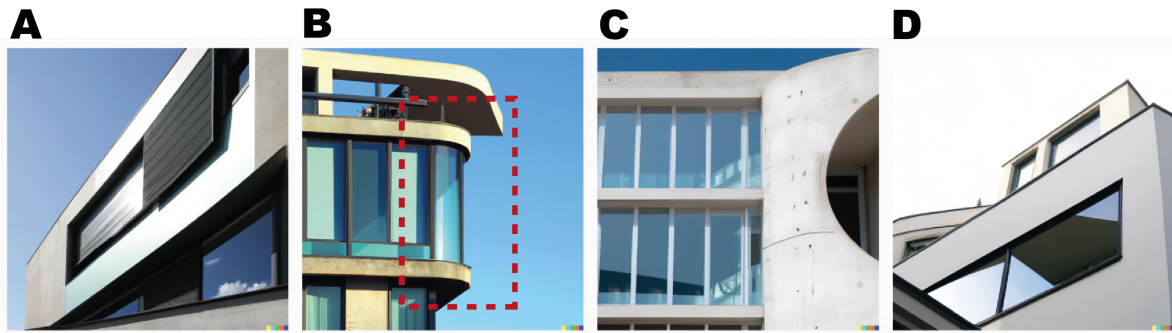


Fig. 41 DALL-E generated images based on the prompt "a modern house with aesthetic windows".

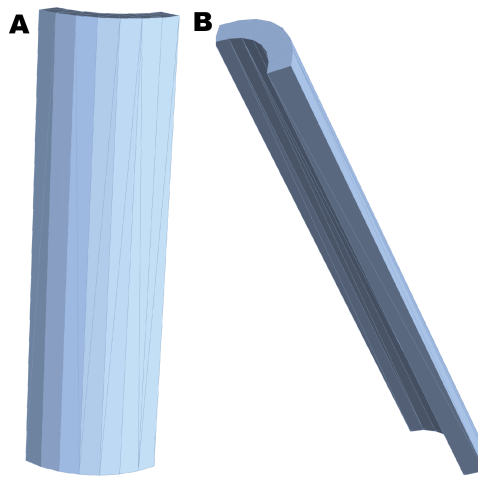


Fig. 42 Model of the aesthetic window depicted in SI Figure 41B. A - forward looking, B - looking from behind.

6.7 LSC Aesthetics

LSCs have been proposed to be more aesthetic than traditional photovoltaics^{74–79}, particularly with application to building integrated photovoltaics^{80–86}. To demonstrate that our simulation can also consider these aesthetic use cases we asked DALL-E, a text-to-image model, for a selection of window designs. Most of the generated windows, those that are rectangular, had already been considered and simulated within the main text (**Main Text Figure 6**). However, **SI Figure 41B**, has a curved window, which we assumed to be approximately 200 cm tall and 50 cm wide. We first generated a model of this window, depicted in **SI Figure 42**. **SI Figure 43** depicts the photon paths of the first 1000 successful photon paths and 100 photons paths within the LSC. We therefore believe our model will be useful to those who wish to design optimised windows for energy capture and those with unique design requirements or visions.

6.8 Further Simulation Results

SI Figures 44 - 50 outline ancillary results from the simulations for the LSCs described in the main text. Specifically the input power incident on the LSC for all LSCs (points are on top of year other) for the Amsterdam spectral model

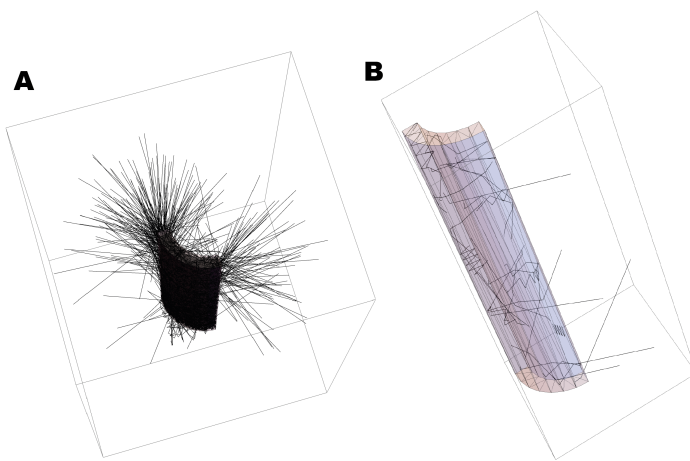


Fig. 43 A - Plot the first 1000 successful photon paths and B - 100 photons paths for the aesthetic LSC

and output power from the LSC (before impinging on the silicon photovoltaic) in 15 minute increments in **SI Figure 44**, LSC PCE before coupling to the silicon photovoltaic for the Amsterdam spectral model and Silicon PCE determined from the LSC output spectrum determined in 15 minute increments throughout the year in **SI Figure 45**, input power incident on the LSC for all LSCs for the Boulder spectral model and output power from the LSC (before impinging on the silicon photovoltaic) in 15 minute increments in **SI Figure 46**, LSC PCE before coupling to the silicon photovoltaic for the Boulder spectral model and Silicon PCE determined from the LSC output spectrum determined in 15 minute increments throughout the year in **SI Figure 47**, modelled device power conversion efficiency (LSC) for a series of LSC designs and a silicon photovoltaic when placed upright on a roof at NREL in Boulder and output energy in kWh in 15 minute increments throughout the year in **SI Figure 48**, input power incident on the LSC for the upright Boulder spectral model and Output power from the LSC (before impinging on the silicon photovoltaic) in 15 minute increments in **SI Figure 49**, and LSC PCE before coupling to the silicon photovoltaic for the upright Boulder spectral model and Silicon PCE determined from the LSC output spectrum determined in 15 minute increments throughout the year in **SI Figure 50**.

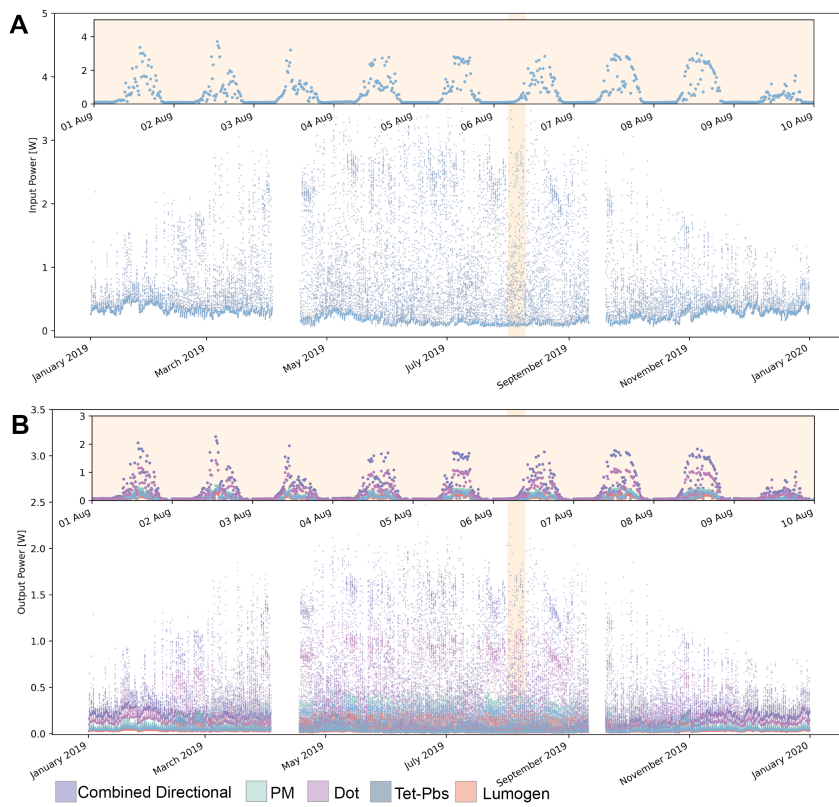


Fig. 44 A - Input power incident on the LSC for all LSCs (points are on top of year other) for the Amsterdam spectral model. B - Output power from the LSC (before impinging on the silicon photovoltaic) in 15 minute increments.

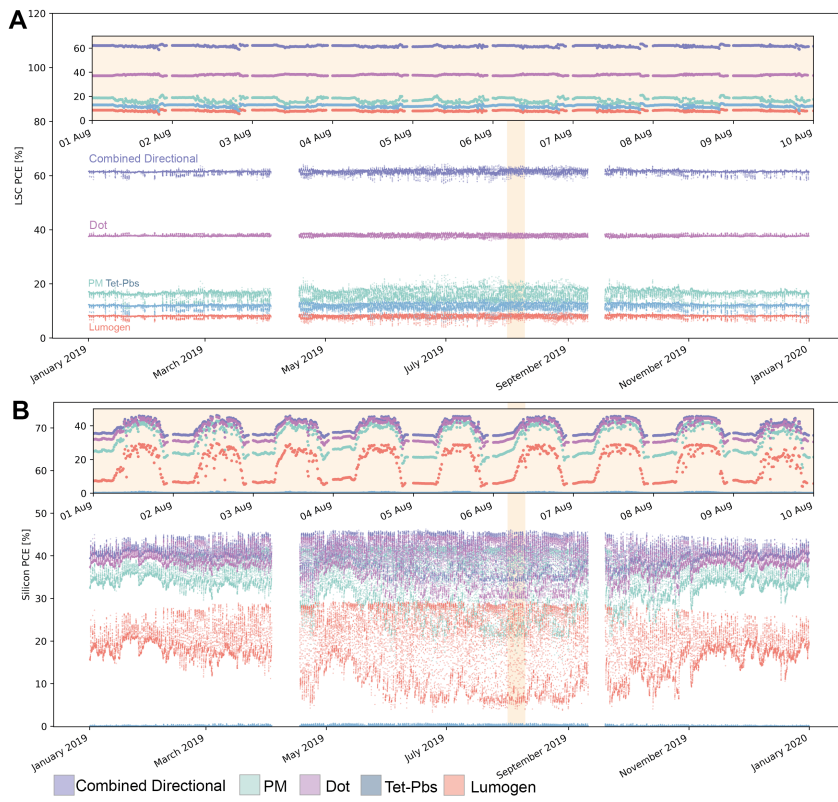


Fig. 45 A - LSC PCE before coupling to the silicon photovoltaic for the Amsterdam spectral model. B - Silicon PCE determined from the LSC output spectrum determined in 15 minute increments throughout the year

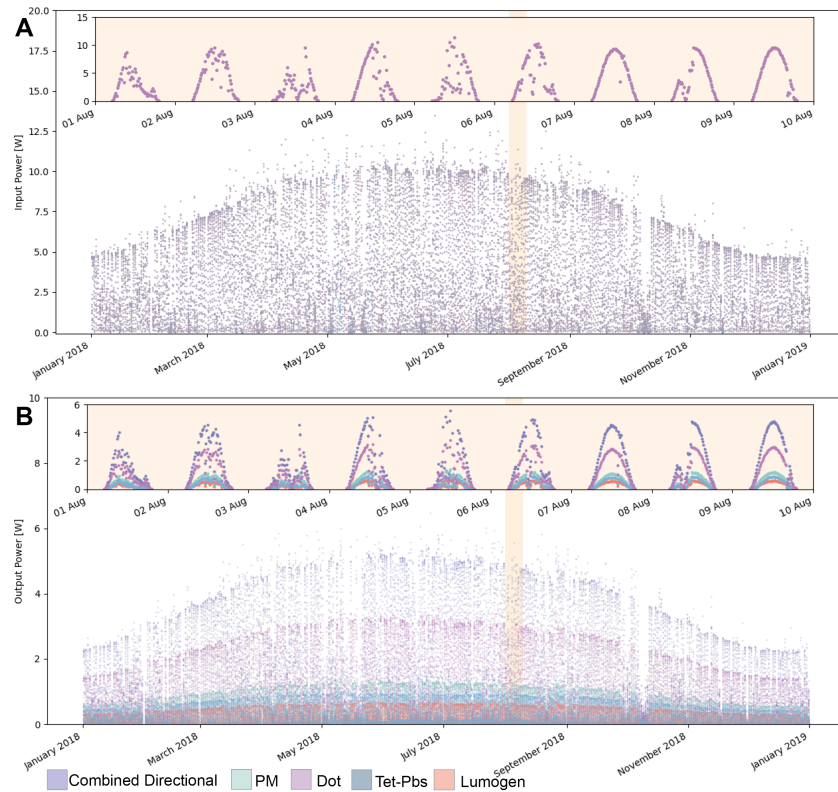


Fig. 46 A - Input power incident on the LSC for all LSCs (points are on top of year other) for the Boulder spectral model. B - Output power from the LSC (before impinging on the silicon photovoltaic) in 15 minute increments.

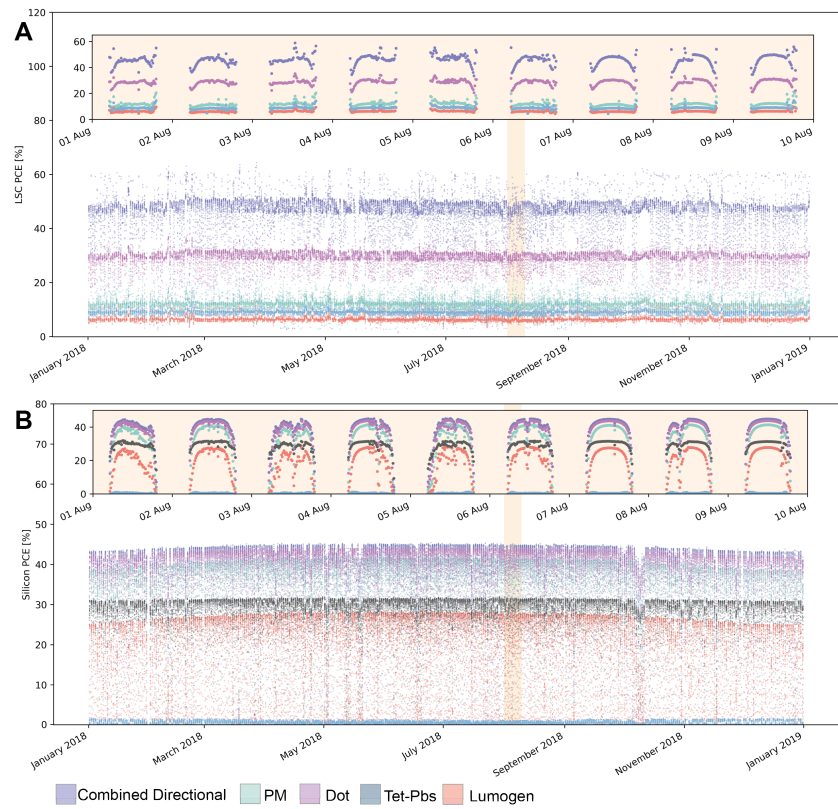


Fig. 47 A - LSC PCE before coupling to the silicon photovoltaic for the Boulder spectral model. B - Silicon PCE determined from the LSC output spectrum determined in 15 minute increments throughout the year

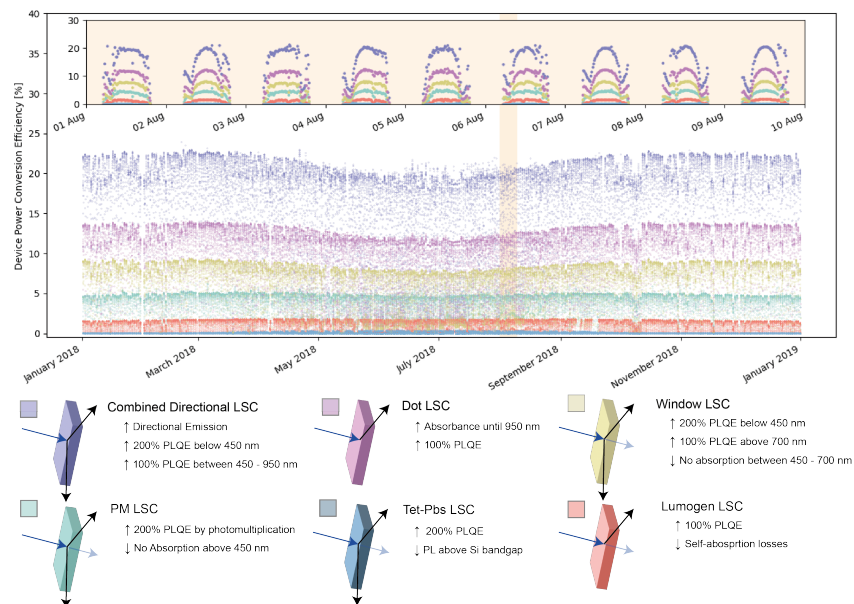


Fig. 48 A - Modelled device power conversion efficiency (LSC) for a series of LSC designs and a silicon photovoltaic (in grey) when placed upright on a roof at NREL in Boulder. B - Output energy in kWh in 15 minute increments throughout the year.

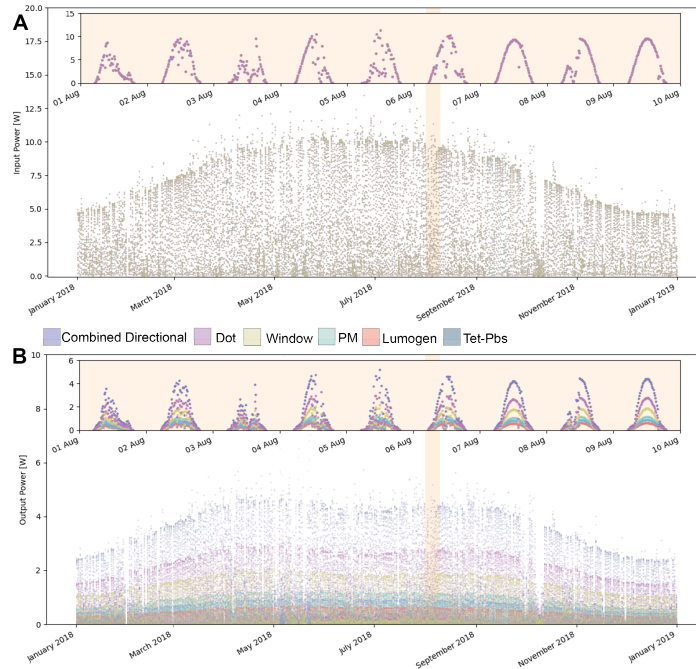


Fig. 49 A - Input power incident on the LSC for all LSCs (points are on top of year other) for the upright Boulder spectral model. B - Output power from the LSC (before impinging on the silicon photovoltaic) in 15 minute increments.

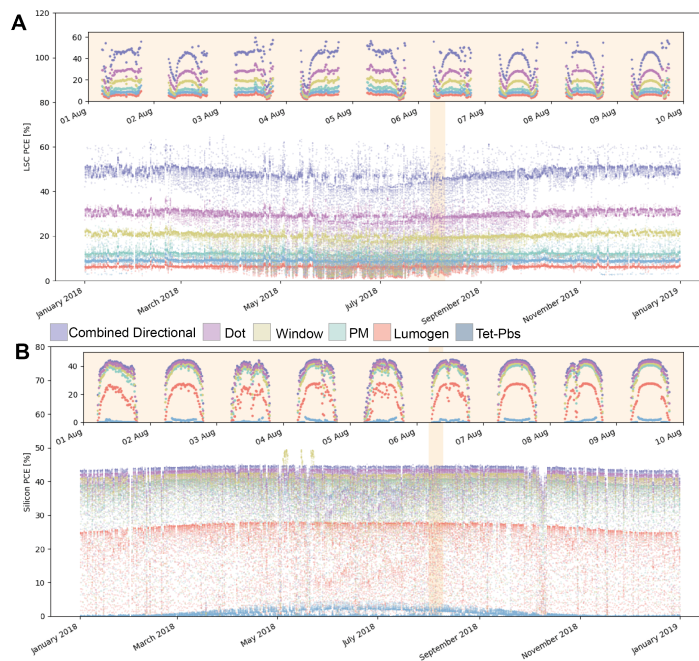


Fig. 50 A - LSC PCE before coupling to the silicon photovoltaic for the upright Boulder spectral model. B - Silicon PCE determined from the LSC output spectrum determined in 15 minute increments throughout the year

7 Derivations for Cost Metric

The power generated given by an area, A_{PV} , of photovoltaic cells is given by

$$A_{\text{PV}} \rho \eta_{\text{PV}} = W_{\text{PV}}, \quad (32)$$

where ρ is the power density of a light source, η_{PV} is the PV cell power conversion efficiency and W_{PV} is the power generated by the cell. In the case of the LSC, the power is given by

$$A_{\text{LSC}} \rho \eta_{\text{LSC}} = W_{\text{LSC}}, \quad (33)$$

where A_{LSC} is the front face area of the LSC, and η_{LSC} is the power conversion efficiency. In the case where the power generated is equal, i.e. $W_{\text{LSC}} = W_{\text{PV}}$, then

$$A_{\text{LSC}} = \frac{A_{\text{PV}} \eta_{\text{PV}}}{\eta_{\text{LSC}}}. \quad (34)$$

Supposing there is a cost constant which is proportional to the area of the module, then the cost to make a PV module is

$$A_{\text{PV}} x, \quad (35)$$

where x is the cost of solar cells per meter squared. Similarly, the cost to make an LSC is,

$$\underbrace{A_{\text{LSC}} y}_{\text{Cost of LSC}} + \underbrace{\frac{A_{\text{LSC}}}{G} x}_{\text{Cost of associated PV}}, \quad (36)$$

where y is the cost per meter square of LSC and G is the geometric factor, which is the area of the top surface (A_{LSC}) divided by the edge area. The constraint for a LSC system to be cheaper than PV is then

$$\left(A_{\text{LSC}} y + \frac{A_{\text{LSC}}}{G} x \right) < A_{\text{PV}} x. \quad (37)$$

Substituting **SI Equation 34** gives

$$\frac{\eta_{\text{PV}}}{\eta_{\text{LSC}}} \left(y + \frac{x}{G} \right) < x. \quad (38)$$

Which can be rearranged to

$$\frac{y}{x} = \frac{\text{Cost of LSC}/m^2}{\text{Cost of PV}/m^2} < \left(\frac{\eta_{\text{LSC}}}{\eta_{\text{PV}}} - \frac{1}{G} \right). \quad (39)$$

SI Figure 51 plots this ratio for the silicon and LSCs described in the main text. Supposing the costs of running an LSC and solar farm may be broadly separated into four parts; property capital cost, PV components, installation and running

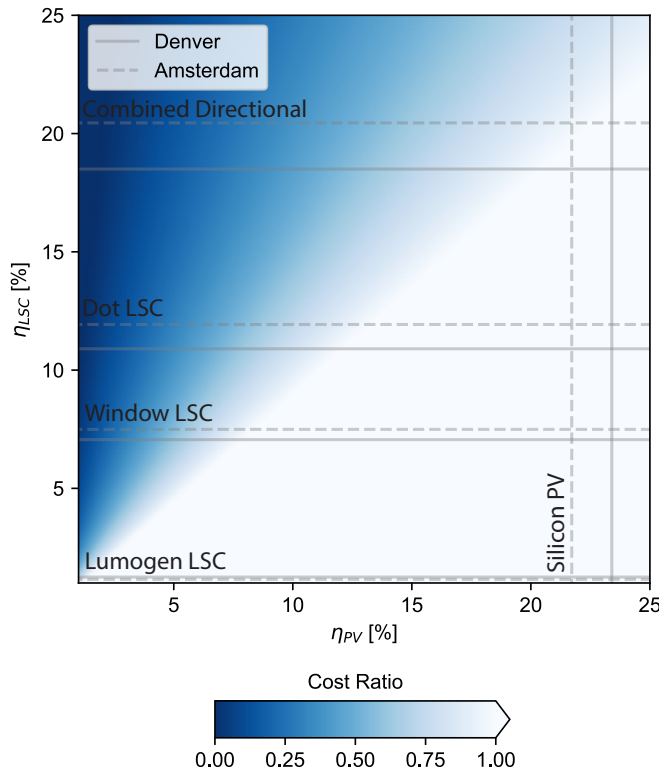


Fig. 51 Plot of SI Equation 39 with efficiencies of silicon PV and select LSCs described in the main text ($G=7.5$). Dashed lines represent the Amsterdam location and solid line represents Denver. Ratio values greater than 1 are not plotted. The closer to zero means the cheaper the cost of the LSC can be per metre squared.

costs. If we further assume the property capital costs of LSC farms and solar farms are approximately equivalent, then this cost reduction must be found in installation, operational or bill of material costs.

Notes and references

- 1 T. K. Baikie, J. Xiao, B. H. Drummond, N. C. Greenham and A. Rao, *ACS Photonics*, 2023.
- 2 T. A. de Bruin and W. G. van Sark, *Ceramics International*, 2023, **49**, 24454–24468.
- 3 M. Phelan, D. R. Needell, H. Bauser, H. Su, M. Deceglie, S. Theingi, B. Koscher, Z. Nett, C. R. Bukowsky, O. Ilic, P. Stradins, J. Geisz, R. Nuzzo, A. P. Alivisatos and H. A. Atwater, *Solar Energy Materials and Solar Cells*, 2021, **223**, 110945.
- 4 N. J. L. K. Davis, R. W. Macqueen, S. T. E. Jones, C. Orofino-Pena, D. Cortizo-Lacalle, R. G. D. Taylor, D. Credgington, P. J. Skabara and N. C. Greenham, *J. Mater. Chem. C*, 1952, **5**, 1952.
- 5 R. Barciela, F. Quintero, A. F. Doval, M. Fernández-Arias, J. del Val, R. Comesaña and J. Pou, *Optics Express*, 2021, **29**, 19566.
- 6 M. Carrascosa, S. Unamuno and F. Agullo-Lopez, *Applied Optics*, 1983, **22**, 3236.
- 7 S. Verma, D. J. Farrell and R. C. Evans, *ACS Applied Optical Materials*, 2023, **1**, 1012–1025.

- 8 D. P. McMeekin, G. Sadoughi, W. Rehman, G. E. Eperon, M. Saliba, M. T. Hörantner, A. Haghhighirad, N. Sakai, L. Korte, B. Rech, M. B. Johnston, L. M. Herz and H. J. Snaith, *Science*, 2016, **351**, 151–155.
- 9 E. Raza and Z. Ahmad, *Energy Reports*, 2022, **8**, 5820–5851.
- 10 *RefractiveIndex.INFO - Refractive index database*, <https://refractiveindex.info/>.
- 11 M. H. Futscher and B. Ehrler, *Efficiency Limit of Perovskite/Si Tandem Solar Cells*, 2016.
- 12 M. H. Futscher and B. Ehrler, *ACS Energy Letters*, 2017, **2**, 2089–2095.
- 13 M. H. Futscher, A. Rao and B. Ehrler, *ACS Energy Letters*, 2018, **3**, 2587–2592.
- 14 K. Yoshikawa, W. Yoshida, T. Irie, H. Kawasaki, K. Konishi, H. Ishibashi, T. Asatani, D. Adachi, M. Kanematsu, H. Uzu and K. Yamamoto, *Solar Energy Materials and Solar Cells*, 2017, **173**, 37–42.
- 15 J. Nelson, *The Physics of Solar Cells*, Imperial College Press, London, 2003.
- 16 W. Shockley and H. J. Queisser, *Journal of Applied Physics*, 1961, **32**, 510–519.
- 17 K. Misiakos and D. Tsamakis, *Journal of Applied Physics*, 1998, **74**, 3293.
- 18 J. Dziewior and W. Schmid, *Applied Physics Letters*, 2008, **31**, 346.
- 19 Y. P. Varshni, *Physica*, 1967, **34**, 149–154.
- 20 S. M. Sze, *Physics of semiconductor devices*, John Wiley & Sons, Inc., New York, 2nd edn, 1981.
- 21 M. V. Orna, *Color Research & Application*, 1985, **10**, 123–124.
- 22 N. Martín and J. M. Ruiz, *Progress in Photovoltaics: Research and Applications*, 2005, **13**, 75–84.
- 23 N. Martin and J. M. Ruiz, *Solar Energy Materials and Solar Cells*, 2001, **70**, 25–38.
- 24 N. Martín and J. M. Ruiz, <http://dx.doi.org/10.1080/01425910212852>, 2010, **22**, 19–31.
- 25 J. Cai and L. Qi, 2015.
- 26 K. X. Wang, Z. Yu, V. Liu, Y. Cui and S. Fan, *Renewable Energy and the Environment Optics and Photonics Congress (2012)*, paper PT2C.2, 2012, PT2C.2.
- 27 E. Yablonovitch, *JOSA*, Vol. 72, Issue 7, pp. 899–907, 1982, **72**, 899–907.
- 28 X. Liu, P. R. Coxon, M. Peters, B. Hoex, J. M. Cole and D. J. Fray, *Energy & Environmental Science*, 2014, **7**, 3223–3263.
- 29 W. Q. Xie, J. I. Oh and W. Z. Shen, *Nanotechnology*, 2011, **22**, 065704.
- 30 X. Luo, T. Ding, X. Liu, Y. Liu and K. Wu, *Nano Letters*, 2019, **19**, 338–341.
- 31 T. A. Cohen, T. J. Milstein, D. M. Kroupa, J. D. Mackenzie, C. K. Luscombe and D. R. Gamelin, *Journal of Materials Chemistry A*, 2019, **7**, 9279–9288.
- 32 C. S. Erickson, M. J. Crane, T. J. Milstein and D. R. Gamelin, *The Journal of Physical Chemistry C*, 2019, **123**, 12474–12484.
- 33 A. Rao and R. H. Friend, *Nature Reviews Materials*, 2017, **2**, 17063.
- 34 N. J. L. K. Davis, J. R. Allardice, J. Xiao, A. J. Petty, N. C. Greenham, J. E. Anthony and A. Rao, *The Journal of Physical Chemistry Letters*, 2018, **9**, 1454–1460.

- 35 V. Gray, J. R. Allardice, Z. Zhang, S. Dowland, J. Xiao, A. J. Petty, J. E. Anthony, N. C. Greenham and A. Rao, *ACS Nano*, 2020, **14**, 36.
- 36 J. R. Allardice, A. Thampi, S. Dowland, J. Xiao, V. Gray, Z. Zhang, P. Budden, A. J. Petty, N. J. Davis, N. C. Greenham, J. E. Anthony and A. Rao, *Journal of the American Chemical Society*, 2019, **141**, 12907–12915.
- 37 B. Daiber, K. Van Den Hoven, M. H. Futscher and B. Ehrler, 2021.
- 38 L. M. Pazos-Outo, J. Min Lee, M. H. Futscher, A. Kirch, M. Tabachnyk, R. H. Friend and B. Ehrler, 2022.
- 39 J. Zhang, H. Sakai, K. Suzuki, T. Hasobe, N. V. Tkachenko, I. Y. Chang, K. Hyeon-Deuk, H. Kaji, T. Teranishi and M. Sakamoto, *Journal of the American Chemical Society*, 2021, **143**, 17388–17394.
- 40 M. A. Green, K. Emery, Y. Hishikawa, W. Warta and E. D. Dunlop, *Progress in Photovoltaics: Research and Applications*, 2011, **19**, 565–572.
- 41 M. A. Green, K. Emery, Y. Hishikawa, W. Warta and E. D. Dunlop, *Progress in Photovoltaics: Research and Applications*, 2012, **20**, 12–20.
- 42 M. A. Green, K. Emery, Y. Hishikawa, W. Warta and E. D. Dunlop, *Progress in Photovoltaics: Research and Applications*, 2012, **20**, 606–614.
- 43 M. A. Green, K. Emery, Y. Hishikawa, W. Warta and E. D. Dunlop, *Progress in Photovoltaics: Research and Applications*, 2016, **24**, 3–11.
- 44 M. A. Green, K. Emery, Y. Hishikawa, W. Warta and E. D. Dunlop, *Progress in Photovoltaics: Research and Applications*, 2016, **24**, 905–913.
- 45 M. A. Green, K. Emery, Y. Hishikawa, W. Warta, E. D. Dunlop, D. H. Levi and A. W. Ho-Baillie, *Progress in Photovoltaics: Research and Applications*, 2017, **25**, 3–13.
- 46 M. A. Green, K. Emery, Y. Hishikawa, W. Warta and E. D. Dunlop, *Progress in Photovoltaics: Research and Applications*, 2015, **23**, 1–9.
- 47 M. A. Green, Y. Hishikawa, E. D. Dunlop, D. H. Levi, J. Hohl-Ebinger and A. W. Ho-Baillie, *Progress in Photovoltaics: Research and Applications*, 2018, **26**, 3–12.
- 48 M. A. Green, K. Emery, Y. Hishikawa, W. Warta and E. D. Dunlop, *Progress in Photovoltaics: Research and Applications*, 2014, **22**, 701–710.
- 49 M. A. Green, Y. Hishikawa, W. Warta, E. D. Dunlop, D. H. Levi, J. Hohl-Ebinger and A. W. H. Ho-Baillie, *Progress in Photovoltaics: Research and Applications*, 2017, **25**, 668–676.
- 50 A. Driemel, J. Augustine, K. Behrens, S. Colle, C. Cox, E. Cuevas-Agulló, F. M. Denn, T. Duprat, M. Fukuda, H. Grobe, G. Hodges, N. Hyett, O. Ijima, A. Kallis, W. Knap, V. Kustov, C. N. Long, D. Longenecker, A. Lupi, M. Maturilli, M. Mimouni, L. Ntsangwane, H. Ogihara, X. Olano, M. Olefs, M. Omori, L. Passamani, B. Pereira, H. Schmithüsen, S. Schumacher, R. Sieger, J. Tamlyn, R. Vogt, L. Vuilleumier, X. Xia, A. Ohmura and G. König-Langlo, *Earth Syst. Sci. Data*, 2018, **10**, 1491–1501.
- 51 Al-Abadi, N (2021): Basic measurements of radiation at station Solar Village (1998-09 to 2002-12), <https://doi.org/10.5281/zenodo.5000000>.

- pangaea.de/10.1594/PANGAEA.932870.
- 52 Vogt, R (2023): *Horizon at station Gobabeb*, <https://doi.pangaea.de/10.1594/PANGAEA.957581>.
- 53 Ramanathan, K (2022): *Horizon at station Gandhinagar*, <https://doi.pangaea.de/10.1594/PANGAEA.947039>.
- 54 Piters, A (2021): *Horizon at station Paramaribo*, <https://doi.pangaea.de/10.1594/PANGAEA.931001>.
- 55 Morel, B; Delsaut, M (2023): *Basic measurements of radiation at station Reunion Island, University (2019-06 et seq)*, <https://doi.pangaea.de/10.1594/PANGAEA.962049>.
- 56 Ijima, O (2010): *Horizon at station Minamitorishima*, <https://doi.pangaea.de/10.1594/PANGAEA.743879>.
- 57 Hodgetts, G et al. (2022): *Basic measurements of radiation at station Camborne (2001-01 et seq)*, <https://doi.pangaea.de/10.1594/PANGAEA.945262>.
- 58 Halliwell, D (2007): *Horizon at station Regina*, <https://doi.pangaea.de/10.1594/PANGAEA.669524>.
- 59 Dutton, EG (2007): *Horizon at station Bermuda*, <https://doi.pangaea.de/10.1594/PANGAEA.669510>.
- 60 L. Xu, F. Xu, J. Liu, X. Zhang, A. S. Subbiah and S. D. Wolf, *ACS Energy Letters*, 2023, 3114–3121.
- 61 T. Masuda, K. Aoyagi, S. Dottermusch, I. A. Howard, B. S. Richards and M. Endo, *Advanced Photonics Research*, 2022, 3, 2100214.
- 62 G. X. de Oliveira, J. O. Lira, D. Cambié, T. Noël, H. G. Riella, N. Padoin and C. Soares, *Chemical Engineering Research and Design*, 2020, 153, 626–634.
- 63 D. Cambié, J. Dobbelaar, P. Riente, J. Vanderspikken, C. Shen, P. H. Seeberger, K. Gilmore, M. G. Debije and T. Noël, *Angewandte Chemie*, 2019, 131, 14512–14516.
- 64 D. Cambié, F. Zhao, V. Hessel, M. G. Debije and T. Noël, *Angewandte Chemie International Edition*, 2017, 56, 1050–1054.
- 65 D. Cambié, F. Zhao, V. Hessel, M. G. Debije and T. Noël, *Reaction Chemistry & Engineering*, 2017, 2, 561–566.
- 66 X. Wang, Y. Zhang, J. Li, G. Liu, M. Gao, S. Ren, B. Liu, L. Zhang, G. Han, J. Yu, H. Zhao, F. Rosei, X. Wang, Y. Zhang, G. Liu, M. Gao, S. Ren, B. Liu, G. Han, H. Zhao, J. Li, L. Zhang, J. Yu and F. Rosei, *Small Methods*, 2022, 6, 2101470.
- 67 G. Panzeri, E. Tatsi, G. Griffini and L. Magagnin, *ACS Applied Energy Materials*, 2020, 3, 1665–1671.
- 68 S. D. Zondag, T. M. Masson, M. G. Debije and T. Noël, *Photochemical and Photobiological Sciences*, 2022, 21, 705–717.
- 69 O. Essahili, O. Lakbita, M. Ouafi and O. Moudam, *Solar Energy*, 2023, 262, 111859.
- 70 C. L. Mulder, L. Theogarajan, M. Currie, J. K. Mapel, M. A. Baldo, M. Vaughn, P. Willard, B. D. Bruce, M. W. Moss, C. E. McLain and J. P. Morseman, *Advanced Materials*, 2009, 21, 3181–3185.
- 71 H.-Y. Huang, K.-B. Cai, P.-W. Chen, C.-A. J. Lin, S.-H. Chang and C.-T. Yuan, *The Journal of Physical Chemistry C*, 2018, 122, 20019–20026.
- 72 I. Papakonstantinou, M. Portnoi and Z. Xu, *Optics Letters*, Vol. 48, Issue 1, pp. 183-186, 2023, 48, 183–186.
- 73 M. Portnoi, P. A. Haigh, T. J. Macdonald, F. Ambroz, I. P. Parkin, I. Darwazeh and I. Papakonstantinou, *Light: Science & Applications* 2021 10:1, 2021, 10, 1–12.

- 74 J. t. Schiphorst, M. L. Cheng, M. van der Heijden, R. L. Hageman, E. L. Bugg, T. J. Wagenaar and M. G. Debije, *Energy and Buildings*, 2020, **207**, 109625.
- 75 Z. Song, Z. Zheng, Y. Zhang, X. Cao, S. Li, H. Zhang, C. Luo, Y. Li and X. Zhang, *Journal of Luminescence*, 2023, **256**, 119622.
- 76 A. Renny, C. Yang, R. Anthony and R. R. Lunt, *Journal of Chemical Education*, 2018, **95**, 1161–1166.
- 77 A. R. Velarde, E. R. Bartlett, N. S. Makarov, C. Castañeda, A. Jackson, K. Ramasamy, M. R. Bergren and H. McDaniel, *ACS Applied Energy Materials*, 2020, **3**, 8159–8163.
- 78 B. Liu, S. Ren, G. Han, H. Zhao, X. Huang, B. Sun and Y. Zhang, *Journal of Materials Chemistry C*, 2021, **9**, 5723–5731.
- 79 F. M. Vossen, M. P. Aarts and M. G. Debije, *Energy and Buildings*, 2016, **113**, 123–132.
- 80 F. Meinardi, F. Bruni and S. Brovelli, *Nature Reviews Materials*, 2017, **2**, 17072.
- 81 P. Moraitis, R. Schropp and W. van Sark, *Optical Materials*, 2018, **84**, 636–645.
- 82 M. G. Debije and P. P. C. Verbunt, *Advanced Energy Materials*, 2012, **2**, 12–35.
- 83 B. S. Richards and I. A. Howard, *Energy & Environmental Science*, 2023.
- 84 J. Son, J. A. Kim, B. S. Joo, W.-Y. Lee, J. Kang, I. K. Han, H. S. Jang, H. Ko and G. Kang, *Solar RRL*, 2023, 2300445.
- 85 A. Boretti, *Advanced Sensor and Energy Materials*, 2023, 100060.
- 86 M. R. Bergren, N. S. Makarov, K. Ramasamy, A. Jackson, R. Guglielmetti and H. McDaniel, *ACS Energy Letters*, 2018, **3**, 520–525.